

# UNIVERSITY OF PADOVA

Department of Physics and Astronomy "Galileo Galilei"

MASTER'S DEGREE IN ASTROPHYSICS AND COSMOLOGY

## Multi-Frequency Study of a Radio Source at the Centre of the Galaxy Cluster Abell S1111

**Supervisor**  
CASSATA PAOLO

**Master Candidate**  
GANDOSI FABRIZIO

**Co-supervisor**  
LOI FRANCESCA

ACADEMIC YEAR 2024-2025

THIS THESIS HAS BEEN DONE IN THE CONTEXT OF THE SCIENTIFIC RESEARCH ACTIVITY OF THE “OSSERVATORIO ASTRONOMICO DI CAGLIARI - ISTITUTO NAZIONALE DI ASTROFISICA”

## Abstract

Active Galactic Nuclei (AGN) are among the most powerful phenomena in the Universe. They play a crucial role in the formation and evolution of galaxies and, in the most powerful cases, in shaping the properties of galaxy clusters.

In this work, I present a study of the BL Lac object PKS 2316-423, located at the centre of the galaxy cluster Abell S1111, using MeerKAT L-band observations. Despite its classification as a blazar, this source exhibits a complex morphology with several features typical of FR I radio galaxies. It hosts a bright, compact core together with very diffuse and filamentary extended emission ( $\sim 400$  kpc), revealed thanks to the high sensitivity and resolution of MeerKAT.

Through in-band spectral mapping, I determined the spectral index distribution with unprecedented resolution. The spectrum steepens from  $\alpha \approx -0.2$  in the core to  $\alpha \approx -1.8$  in the outermost regions of the lobes ( $S_\nu \propto \nu^\alpha$  with  $S_\nu$  being the flux density). Fitting a Jaffe–Perola model to these results yields radiative ages ranging from  $\sim 25$  to 120 Myr.

A polarimetric analysis provides further insight into the source properties and its interaction with the surrounding intracluster medium. Rotation measure synthesis reveals evidence of the Laing–Garrington effect, contributing to the characterization of the source and offering a means to constrain the strength and structure of the magnetic field in the intervening environment.

# Contents

<b>1</b>	<b>Introduction</b>	<b>4</b>
<b>2</b>	<b>Active Galactic Nuclei</b>	<b>6</b>
2.1	AGN unification scheme . . . . .	7
2.2	Radio quiet and radio loud AGN . . . . .	9
2.3	Blazars . . . . .	12
<b>3</b>	<b>AGN role in Galaxy Clusters</b>	<b>15</b>
3.1	Galaxy Clusters . . . . .	15
3.2	AGN feedback . . . . .	17
<b>4</b>	<b>PKS 2316-423 and its Cluster Environment</b>	<b>19</b>
<b>5</b>	<b>Radio Astronomical Background</b>	<b>23</b>
5.1	Synchrotron Radiation . . . . .	23
5.2	Faraday Rotation and depolarization . . . . .	25
5.3	Fundamental Quantities in Radio Astronomy . . . . .	27
5.4	Radio Telescopes . . . . .	28
5.4.1	Single dish . . . . .	29
5.4.2	Radio Interferometry . . . . .	30
<b>6</b>	<b>Observations and data reduction</b>	<b>33</b>
6.1	Observations . . . . .	33
6.2	Data reduction and imaging . . . . .	34
6.2.1	From calibration to imaging . . . . .	34
6.2.2	Imaging . . . . .	35
<b>7</b>	<b>Data Analysis</b>	<b>39</b>
7.1	Morphology . . . . .	39
7.2	Spectral Analysis . . . . .	41
7.2.1	In-band MeerKAT Spectral Index . . . . .	41
7.2.2	Integrated Spectral Index . . . . .	44
7.2.3	Spectral Ageing . . . . .	46
7.3	Polarization analysis . . . . .	51
7.3.1	Rotation Measure Synthesis . . . . .	52
<b>8</b>	<b>Conclusions</b>	<b>61</b>
	<b>References</b>	<b>63</b>

## Introduction

Active Galactic Nuclei (AGN) are among the most powerful phenomena in the universe. Powered by accretion onto supermassive black holes at the centres of galaxies, they release enormous amounts of energy across the whole electromagnetic spectrum. This energy often drives relativistic jets that propagate far beyond the stellar body of the host galaxy, transporting energy and matter into the intergalactic medium which shapes their large-scale environments and regulates galaxy evolution through feedback processes. Understanding the physics of AGN jets and their interaction with the surrounding medium is therefore a central question in modern astrophysics.

Within the AGN unification scheme framework, the different morphologies and many electromagnetic properties of these object can be explained by the orientation from which are observed. In particular, BL Lacs objects are part of the Blazar class and are interpreted as radio-loud AGN whose relativistic jets are closely aligned with the line of sight. This orientation leads to strong relativistic beaming, which boosts the observed jet emission while suppressing extended structures such as radio lobes. As a result, BL Lacs are generally associated with compact morphologies and tend to be core-dominated in the GHz regime.

Nevertheless, recent low frequency observations with LOFAR (Mooney et al., 2021), revealed that most of these objects present an extended emission, with a median spatial extent of  $\sim 70$  kpc, and median spectral index of  $\alpha \sim -0.3$ , with  $S_\nu \propto \nu^\alpha$ .

Characterizing the extended emission from Blazars can help to explain some of the questions regarding these objects such as the relationship between the jet power and the AGN accretion rate and the interplay between the diffuse radio emission and the surrounding environment.

In this thesis, I investigate the case of a BL Lac object that displays unexpectedly extended radio emission. Using high-sensitivity and wide-bandwidth data from MeerKAT L-band radio observations, we perform a spectro-polarimetric analysis of its jets and lobes. Our aim is to characterize the morphology, spectral behaviour and ageing, as well as polarization properties of the source, placing these results in the broader context of AGN unification and jet–environment interactions. Through this work, we highlight the potential of new-generation radio interferometers to uncover faint, extended structures in blazar populations, and we address their implications for the physics of AGN feedback and the evolution of radio-loud galaxies.

This thesis is organized as follows.

Section 2 introduces the theoretical background of AGN, the unification scheme, and the distinction between radio-quiet and radio-loud AGN, with a particular focus on the blazar subclass. Section 3 reviews galaxy clusters and the role of AGN in their environments, including the main feedback mechanisms. Section 4 presents the literature on the target of this study, providing its multi-frequency observational background. Section 5 summarizes key concepts in radio astronomy relevant to the analysis. Section 6 describes the reduction

of the MeerKAT dataset and the production of science-ready images. Section 7 presents the morphological, spectral, and polarimetric analyses, including the effect of the intracluster medium on the polarized emission. Finally, Section 8 summarizes the main findings of this work and discusses future prospects.

## Active Galactic Nuclei

This chapter presents the theoretical framework behind Active Galactic Nuclei, outlines their principal observational properties, and places particular emphasis on radio observations and blazars, given the target of this thesis.

Active Galactic Nuclei are compact regions at the centres of galaxies that emit extraordinary amounts of energy across the entire electromagnetic spectrum, powered by the accretion of matter onto a supermassive black hole (SMBH). Their emission often exceeds that of the combined stellar population of the host galaxy and is characterized by phenomena such as relativistic jets, strong variability, and the presence of broad and narrow emission lines.

The concept of Active Galactic Nuclei dates back to the discovery of unusually bright galactic cores. The first evidence was presented by Seyfert (1943), who reported the presence of broad and strong emission lines in the spectra of a class of spiral galaxies which are now classified after its name. A few decades later, the detection of intense radio sources associated with distant galaxies (e.g., 3C 273 (Schmidt, 1963)) revealed the extragalactic nature and extreme luminosity of these objects.

These discoveries marked the birth of AGN studies and established that their immense energy output could not be explained by stellar processes alone.

Today, AGN are understood as systems powered by accretion onto a supermassive black hole with masses in the range  $10^6$ – $10^{10} M_{\odot}$  (Kormendy and Ho, 2013). As matter falls into the black hole, gravitational energy is released and converted into radiation or, in some cases, into powerful outflows of relativistic plasma.

AGN present unique observational signatures over more than twenty orders of magnitude in frequency, from low-frequency radio waves to high-energy gamma rays (Padovani et al., 2017).

Radio emission provides a key tracer of these systems. At such frequencies, radiation arises from both thermal and non-thermal processes. Thermal radio emission is typically linked to star formation, through mechanisms such as free–free radiation in H II regions and synchrotron emission from supernova remnants, and is therefore confined to the stellar body of galaxies. By contrast, non-thermal radio emission is dominated by synchrotron radiation associated with AGNs, produced by relativistic particles accelerated in the vicinity of the SMBH. This process can generate powerful outflows and collimated jets that extend far beyond the galactic scale, reaching hundreds of kiloparsecs or even megaparsecs into the surrounding medium.

The following sections present an outline of the AGN classification, with the objective of narrowing down to more specific categories, ultimately arriving at the one that includes the target of this thesis.

## 2.1 AGN unification scheme

A wide variety of observational classes has been identified over the decades, creating what has been named the "AGN zoo" by Padovani et al. (2017). These objects differ in their optical spectra (presence or absence of broad emission lines), in their radio loudness, in their infrared properties, and in their higher energies behaviour.

However, much of this diversity can be understood if we work in the framework of the AGN unification scheme, which proposes that the observed properties differs mainly due to orientation effects, rather than intrinsic physical differences (Antonucci, 1993; Urry and Padovani, 1995). Within this framework, all AGN are thought to share a common physical structure around the central SMBH. The core region can be decomposed into several components that account for the wide variety of morphologies and spectral properties observed across the electromagnetic spectrum. Most of these components cannot be directly resolved with current instrumentation and their existence is inferred from indirect observational evidence. Following this model, the inner structure of an AGN can be schematically represented as shown in Figure 1.

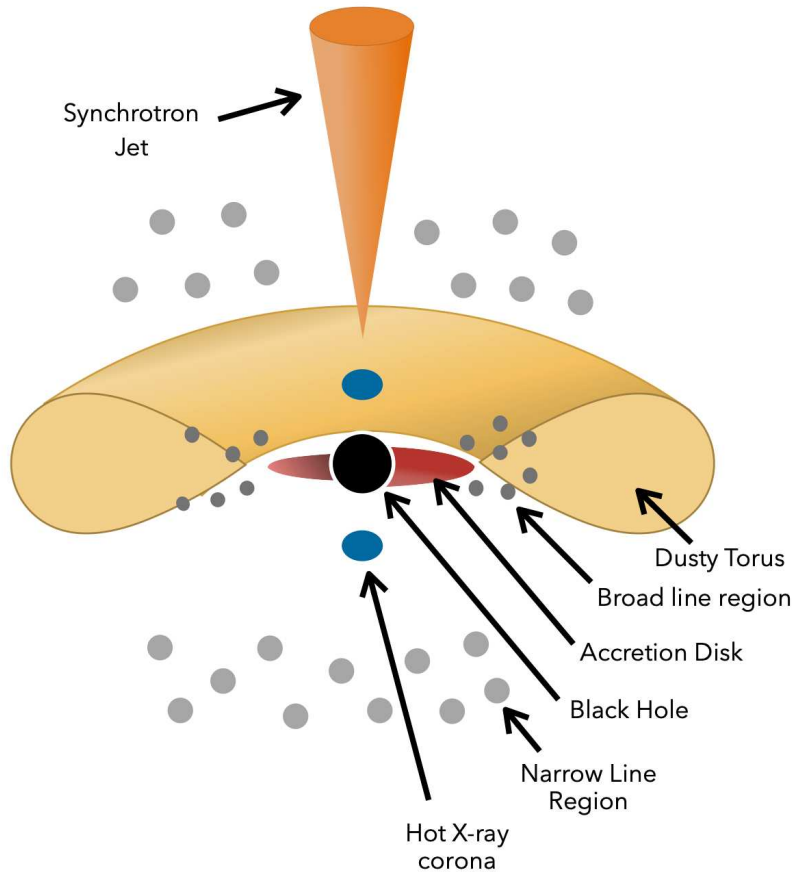


**Figure 1.** Inner structure of an AGN according to the unification theory. Credits J.E. Thorne.

We can identify several components:

- **Supermassive Black Hole:** At the centre of every AGN lies a supermassive black hole, with masses typically ranging from  $10^6$  to  $10^{10} M_{\odot}$ . Although the black hole itself does not emit radiation directly, its gravitational influence is the fundamental driver of all the emission and acceleration of particles.

- **Accretion Disk:** Surrounding the SMBH is a geometrically thin, optically thick accretion disk composed of infalling gas and dust. The disk is heated up to temperature of  $10^6$  K through viscous dissipation of gravitational potential energy as material spirals inward, producing thermal emission peaking in the optical–UV range. This component is the primary source of ionizing photons that excite surrounding gas clouds and is also responsible for the ejection of the jet via magnetohydrodynamical (MHD) effects.
- **Corona:** Located just above and below the accretion disk, the corona is a hot, diffuse region of highly energetic electrons ( $T \sim 10^9$  K). It Compton up-scatters lower-energy photons from the disk into the X-ray regime, producing the characteristic X-ray power-law continuum observed in many AGN. The corona is also thought to be the main contribution to the variability of the X-ray emission on short timescales.
- **Broad Line Region (BLR):** Located just beyond the accretion disk, the BLR consists of high-density gas clouds ( $n_e \sim 10^9 - 10^{11} \text{ cm}^{-3}$ ) moving at high velocities (thousands of km/s). These clouds are photoionized by the accretion disk and produce Doppler-broadened emission lines in the optical and UV spectra.
- **Obscuring Torus:** Encircling the accretion disk and BLR at larger radii (a few parsecs), the torus is a thick, dusty structure that absorbs UV and optical radiation and re-emits it in the infrared. It plays a central role in the AGN unification model, as its orientation determines whether we see broad emission lines.
- **Narrow Line Region (NLR):** Situated further out from the nucleus (tens to hundreds of parsecs), it consists of low-density gas ( $n_e \sim 10^3 \text{ cm}^{-3}$ ) moving at slower velocities (a few hundred km/s). It emits narrow optical and UV emission lines due to the same mechanism of the BLR.
- **Jet:** Present in radio-loud AGN, these highly collimated outflows of plasma are launched perpendicular to the accretion disk via magnetohydrodynamic processes, possibly involving the Blandford–Znajek (Blandford and Znajek, 1977) or Blandford–Payne (Blandford and Payne, 1982) mechanisms. Jets can extend from parsec to megaparsec scales, emit synchrotron radiation across the electromagnetic spectrum, and are responsible for the characteristic radio lobes in radio galaxies and the beamed emission in blazars.

Figure 2 reports the most common combinations of BH activity and view angle, leading to the most used classifications. In the bottom part we can find the radio quiet AGN, above the radio loud.

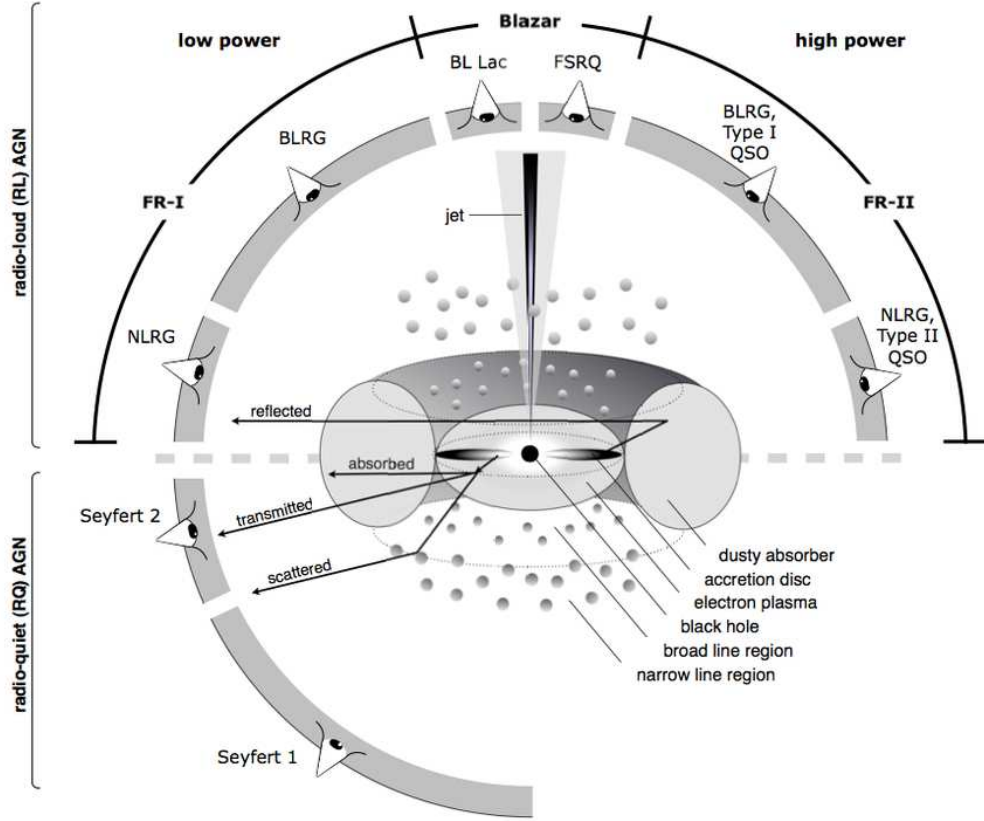


**Figure 2.** Schematic representation of our understanding of the AGN phenomenon in the unified scheme. The type of object we see depends on the viewing angle, whether or not the AGN produces a significant jet emission, and how powerful the central engine is. Credits Marie-Luise Menzel (Beckmann and Shrader, 2012).

## 2.2 Radio quiet and radio loud AGN

One of the most fundamental distinctions among AGN is based on their radio emission. A simple dividing line can be drawn by considering their total radio power, or equivalently the ratio between radio and optical emission (Kellermann et al., 1989). Objects with strong radio emission, often accompanied by large-scale jets and lobes, are classified as *radio-loud*, whereas those with comparatively weak or absent extended radio emission are defined as *radio-quiet*.

This dichotomy has profound implications for understanding the physics of AGN, since it reflects differences in jet production, accretion modes, and host galaxy environments.

**Radio quiet AGN** Among the radio quiet AGN population, Seyfert galaxies are the most common manifestation, divided in two sub-classes, Seyfert 1 and 2. The difference between the two classes is based on the presence of broad permitted lines ( $v \sim 10$  km/s) and narrow forbidden lines ( $v \sim 1$  km/s) in Seyfert 1, while only narrow lines in the Seyfert 2 have been observed. The cause of this distinction is considered to be the orientation at which we observe the nucleus.

By looking at a shallow angle with respect to the axis of rotation, we can directly see the inner part of the core, including the broad line region and the accretion disk. The optical spectrum is therefore dominated by strong, Doppler-broadened emission lines originating

from high-velocity ionized gas in the broad-line region, as well as a variable continuum produced by the hot accretion disk. Moreover, an unobscured line of sight allows us to detect both soft and hard X-ray emission originating from the hot corona above the accretion disk. The X-ray spectrum is typically characterized by a power-law continuum, a Fe  $K\alpha$  emission line at 6.4 keV, and reflection features, often accompanied by rapid variability that traces the innermost regions of the active nucleus.

If we instead increase the angle of observation, getting closer to the plane of the accretion disk, we start to observe the effect of the dusty torus, in fact it is no longer possible to directly see the BLR, as it becomes obscured by optically thick dust and gas. This causes a decrease in the UV and soft X-ray emission but a consequent increase in the IR part of the spectrum.

**Radio loud AGN** In contrast to their radio-quiet counterparts, radio-loud AGN present very extended non-thermal synchrotron emission, mainly visible at radio frequencies.

The outflow usually extends way beyond the stellar radius of the galaxies and, at these scales, this emission is typically structured into four main components, shown in Figure 4:

- **Core** – The central region of the galaxy, associated with the supermassive black hole and accretion processes. In almost all observations, except in some high resolution ( $\sim$ milliarcseconds) studies, it appears as a bright unresolved source.
- **Jets** – Narrow, highly collimated streams of relativistic particles ejected from the core, often extending well beyond the host galaxy.
- **Plumes (or Lobes)** – Large, diffuse regions formed as the jets deposit energy and relativistic particles into the surrounding medium.
- **Hotspots** – Bright, compact regions usually located at the jet termination points or along the inner jets, where strong shocks accelerate particles as the jets interact with the environment.

The physical origin of these large-scale jets is generally attributed to MHD processes near the central engine. Two widely discussed mechanisms are the *Blandford–Znajek* process (Blandford and Znajek, 1977), in which energy is extracted from the rotational spin of the black hole through magnetic field lines threading the event horizon, and the *Blandford–Payne* mechanism (Blandford and Payne, 1982), where centrifugal forces along magnetic field lines anchored in the accretion disk launch plasma outflows.

In both of these models, the magnetic field lines should move outwards in an helical way, as shown in the schematic (Marscher et al., 2008) and the image of M87 (Pasetto et al., 2021) in Figure 3.

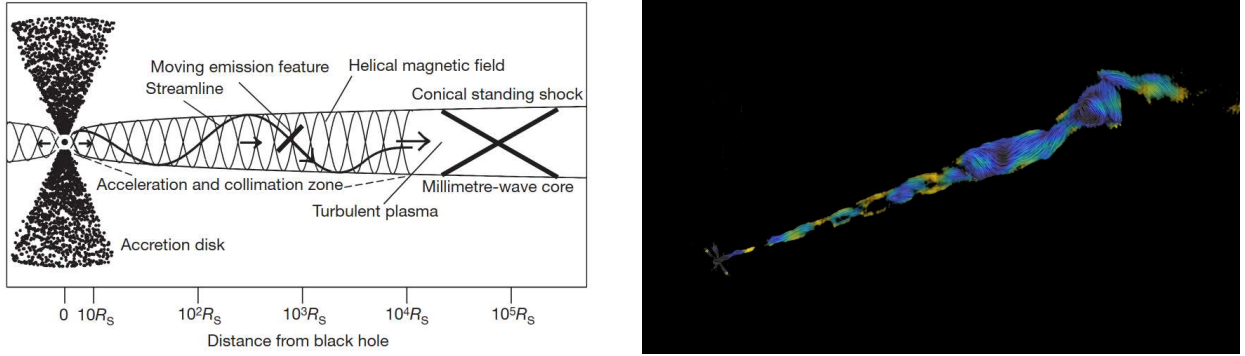


**Figure 3.** *Left:* schematics of the morphology in the inner part of the jet, showing double helical magnetic field lines (Marscher et al., 2008). *Right:* polarization image in the conical jet of M87, revealing a helical magnetic field configuration (Pasetto et al., 2021).

Depending on whether the AGN is in a low or high power regime, we can find the most famous dichotomy of radio loud AGN: the Fanaroff-Riley classification (Fanaroff and Riley, 1974).

In their work, Fanaroff and Riley divided radio galaxies into two classes based on the relative brightness of their jets and lobes, a scheme that also correlates with the total radio power of the source. Originally the classification distinguished only two types, but with increasing sensitivity and angular resolution, refinements have been introduced to account for the diversity of morphologies, accretion modes, and environments (e.g. Baldi et al. (2015); Stroe et al. (2022)). Today, most radio galaxies can still be described within the following framework:

- **FR I** – These sources exhibit edge-darkened radio morphologies, where the surface brightness decreases away from the core. Their jets are typically decollimated and disrupted at short distances from the nucleus, forming turbulent plumes rather than extended lobes. FR I galaxies have low radio power (typically below  $\sim 10^{25} \text{ W Hz}^{-1}$  at 1.4 GHz), are usually found in rich clusters, and are hosted by giant elliptical galaxies. They are associated with low-excitation optical spectra and radiatively inefficient accretion flows, often fuelled by hot gas from the intra-cluster medium (Saripalli, 2012).
- **FR II** – These sources display edge-brightened morphologies, with well-collimated jets terminating in bright hotspots and extended lobes. Their radio power exceeds  $\sim 10^{25} \text{ W Hz}^{-1}$  at 1.4 GHz. FR II galaxies are found in more isolated environments and are generally hosted by less massive ellipticals, often undergoing mergers. They tend to show high-excitation emission lines and are powered by radiatively efficient, cold-mode accretion from reservoirs of molecular gas. Their symmetry and collimation suggest that the jets remain relativistic out to large distances (Saripalli, 2012).

This difference is easy to see by comparing these two type of radio galaxy side by side, as presented in Figure 4, that shows their most common components.

The Fanaroff–Riley dichotomy thus highlights how radio power, accretion mode, and jet dynamics combine to shape the large-scale radio morphology of AGN. Although many variations and sub-classes have been proposed, the FR classification remains a cornerstone for understanding radio-loud AGN.

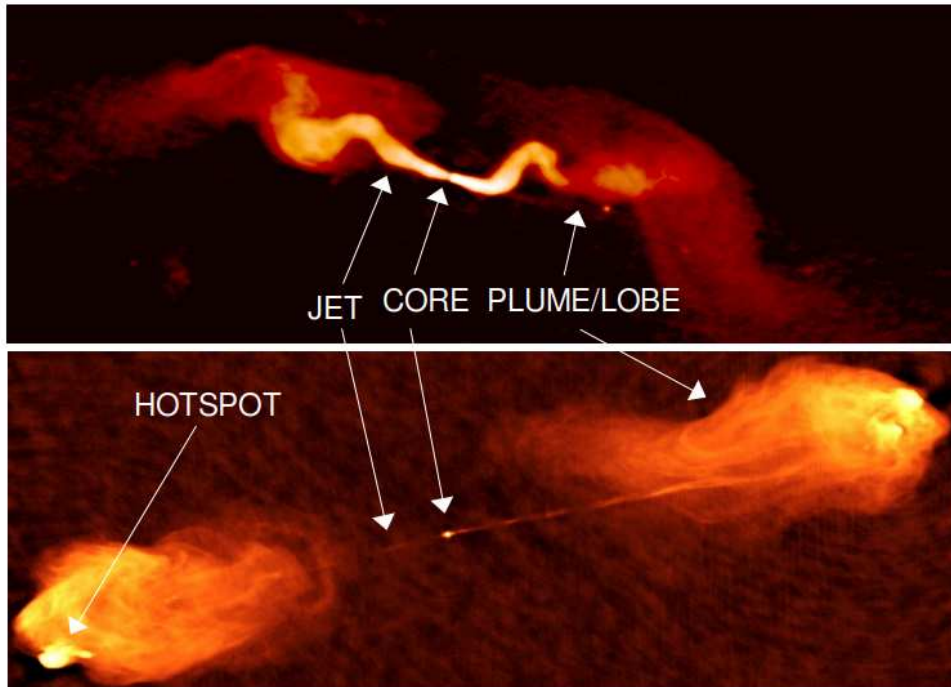


**Figure 4.** *Top:* Picture of 3C31, a classical example of FR I radio galaxy (Laing et al., 2008). *Bottom:* Picture of Cygnus-A, a FR II radio galaxy (Alexander et al., 1984).

## 2.3 Blazars

This section presents an overview of blazars, contextualizing the object presented in this work.

Blazars represent the most extreme manifestation of radio-loud AGN. For these sources, a relativistic jet is closely aligned with our line of sight, and the emission is strongly amplified by Doppler boosting, causing them to appear exceptionally luminous and variable.

Blazars are observed across the entire electromagnetic spectrum, from radio waves to gamma rays.

They are traditionally divided into two subclasses:

- **Flat-Spectrum Radio Quasars (FSRQs)** – These display strong and broad optical emission lines, typically associated with high accretion rates and prominent broad line regions.
- **BL Lacertae Objects (BL Lacs)** – These show weak or absent emission lines, suggesting a low-luminosity accretion disk and a less prominent broad line region.

In both cases, their broadband spectral energy distribution (SED) is characterized by two broad components: a low-energy hump peaking between the infrared and X-ray bands, generally attributed to synchrotron emission from relativistic electrons in the jet, and a high-energy hump extending into the gamma-ray regime, produced by inverse Compton scattering of low-energy photons with the relativistic electrons present in the jets (namely Synchrotron Self Compton, or SSC).

An example of this spectrum is presented in Figure 5, obtained from the work by Padovani

and Giommi (1995) and shows the different spectrums of the so called *blazar sequence*, where the blazar SED depends mostly on the intrinsic luminosity and the position of the first peak.

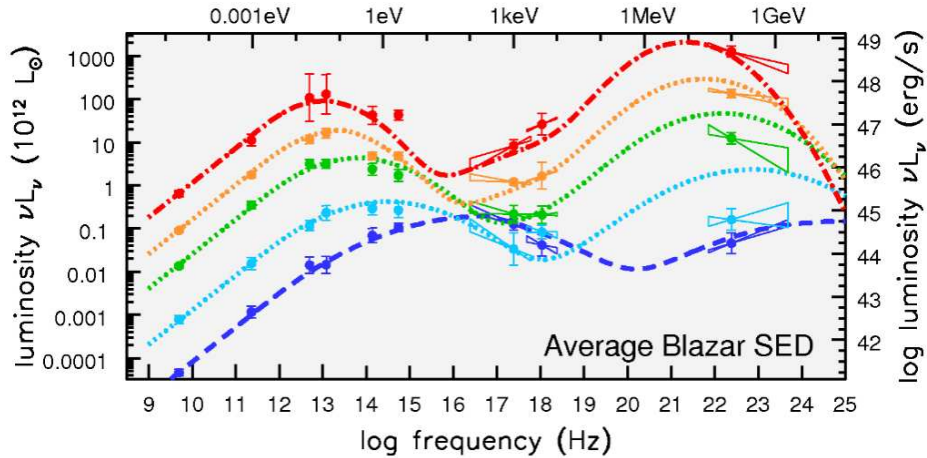


**Figure 5.** The plot shows the double-hump structure characteristic of blazars, with synchrotron emission peaking in the IR to X-ray regime and inverse Compton emission dominating at higher energies. Different colours correspond to blazars with decreasing radio luminosity, and dashed/dotted lines represent empirical model fits to the observed data points (Padovani and Giommi, 1995).

From a radio perspective, blazars are characterized by compact, flat-spectrum cores ( $-0.5 < \alpha < 0.5$ , where the flux density  $S_\nu \propto \nu^\alpha$ ) dominated by synchrotron emission from the relativistic jet. High-resolution observations reveal that these cores often contain one-sided parsec-scale jets, an effect of relativistic beaming that enhances the approaching jet while suppressing the receding counterpart.

On larger scales, blazars typically show a morphological connection with the Fanaroff–Riley classification: BL Lac objects are predominantly associated with FR I-like extended radio structures, whereas FSRQs are typically linked to FR II-like morphologies.

However, more recent results found hybrid morphology, suggesting that the division lies rather between low- and high-excitation radio galaxies (Pajdosz-Śmierciak et al., 2022).

The dominance of the compact, beamed jet introduces some selection biases: blazars are often identified through flat-spectrum radio catalogues or high-energy  $\gamma$ -ray surveys, which preferentially pick out the most core-dominated sources (Massaro et al., 2015). The extended emission is often faint and projection effects shorten the observed structure. As a consequence, the large-scale, diffused structures that would otherwise connect them to the Fanaroff–Riley classes are frequently faint or entirely undetected.

However, deep radio imaging has shown that extended emission in blazars is not uncommon, especially at lower frequencies (Mooney et al., 2021). Very Large Array (VLA) and Low Frequency array (LOFAR) studies reveal that a significant fraction of BL Lac objects exhibit kiloparsec-scale radio structures, including lobes and plumes reminiscent of FR I radio galaxies (Cassaro, P. et al., 1999), with a median extent of  $\sim 69 \pm 4$  kpc reported in the work of Mooney. Similarly, FSRQs are morphologically associated with FR II-like morphologies (Kharb et al., 2010).

These results support the idea that blazars and radio galaxies are intrinsically the same class of objects, with orientation and relativistic beaming accounting for the observed differences, as predicted by the unification scheme.

For these reasons, blazars provide a unique laboratory: they allow us to probe both the compact, Doppler-boosted inner jets on parsec scales through Very Long Baseline Interferometry (VLBI), and, where sensitivity allows, the extended emission on kiloparsec scales. The interplay between these two regimes, compact core and extended lobes, forms a key part of understanding jet physics, AGN feedback, and the evolutionary connection between blazars and their parent radio galaxies.

## AGN role in Galaxy Clusters

This chapter aims to place AGN within their most common environment, galaxy clusters. Section 3.1 provides an overview of these massive systems, while Section 3.2 discusses the continuous interplay between AGN and their environment.

### 3.1 Galaxy Clusters

Galaxy clusters are the most massive gravitationally bound objects in the Universe, containing up to thousands of galaxies and having masses up to  $10^{14}$ - $10^{15}$  solar masses. Their composition is dominated by dark matter ( $\sim 80\%$ ), with 15-17% of their mass coming from the ionised plasma of the intracluster medium (ICM) and only 3-5% from the stars of their galaxies and cold gas (Dekel and Ostriker, 1999).

Although dark matter has not been directly detected at any wavelength and its nature remains unknown, its amount and distribution in clusters can be inferred from optical observations. An interesting example of the distribution of elements in galaxy clusters can be found in the Bullet Cluster, presented in Figure 6.



**Figure 6.** The image shows the central region of the Bullet Cluster, which is made up of two massive galaxy clusters. The near infrared image captured by NASA's James Webb Space Telescope shows the vast amount of galaxies and gravitational lensing. Glowing, hot X-rays captured by Chandra X-ray Observatory appear in pink while the blue represents the dark matter. Credit NASA.

In the hierarchical scenario of structure formation, clusters form through the merger of smaller units such as groups and sub-clusters. These mergers are among the most energetic events in the Universe, releasing kinetic energies of up to  $\sim 10^{64}$  erg (Sarazin, 2002). A significant fraction of this energy is dissipated into the ICM, driving shocks, turbulence, and bulk motions that heat the gas.

These characteristics can be probed with X-ray observations, from the early Einstein,

ROSAT, and ASCA missions to the more recent Chandra, eROSITA, and XMM-Newton, which allow us to trace the global cluster gravitational potential and investigate their dynamics, morphology, and evolutionary history.

A complete physical description of the ICM also requires accounting for its non-thermal components (van Weeren et al., 2019), best revealed through radio observations. Many clusters host diffuse synchrotron sources —radio halos, relics, and mini-halos— that are not directly associated with individual galaxies but instead trace the ICM itself. The synchrotron emission implies the presence of relativistic ( $\sim$ GeV) electrons and cluster magnetic fields at the  $\mu$ G level which get accelerated and amplified by some of the energy released in the ICM. Independent evidence for such magnetic fields comes from Faraday rotation measure studies of radio galaxies located within or behind clusters (this is presented in Section 5.2). Cluster magnetic fields play an important role in particle acceleration processes. Additionally, magnetic fields inhibit transport processes like heat conduction, spatial mixing of gas, and the propagation of cosmic rays.

Further confirmation of relativistic particles in the ICM comes from detections of non-thermal inverse Compton (IC) emission in the hard X-ray and possibly extreme ultraviolet bands. By combining diffuse radio synchrotron emission with hard X-ray IC measurements, it is possible to constrain the strength of intracluster magnetic fields (Govoni et al., 2002). Magnetic fields in clusters are not only dynamically relevant for the ICM but also play a fundamental role in regulating galaxy evolution within these environments. They can influence star formation, affect the transport of cosmic rays and thermal conduction, and shape the propagation of AGN jets and radio lobes (Fabian, 2012).

A direct observational evidence of the impact of magnetic fields in single galaxies is given by the jellyfish galaxies, where strong, highly ordered magnetic fields favour star formation (Muller et al., 2021).

Moreover, magnetic fields impact the efficiency of feedback processes, as they guide and confine relativistic outflows, thereby affecting the heating of the ICM and the suppression of cooling flows (Su et al., 2019).

Galaxy clusters typically reside in the highest-density regions of the cosmic web, corresponding to the deepest gravitational potential wells. In contrast, low-density regions are populated by poor groups and isolated galaxies, some of which may not belong to any detectable association (Einasto, Maret et al., 2024). Within the hierarchical model of structure formation, galaxy groups and sub-clusters represent the fundamental building blocks of the most massive cosmological structures. Investigating their properties is therefore essential to understanding the formation and evolution of large-scale structure, as well as the origin and amplification of cosmic magnetic fields.

In summary, galaxy clusters provide unique laboratories for studying both the thermal and non-thermal components of baryonic matter on the largest scales. Their hot intracluster medium, coupled with relativistic particles and magnetic fields, reflects a complex balance between gravitational dynamics, plasma processes, and astrophysical feedback. Understanding these environments is therefore essential not only for probing the physics of large-scale structure formation, but also for constraining the role of active galactic nuclei and cosmic magnetism in shaping the Universe.

## 3.2 AGN feedback

Active Galactic Nuclei are not only spectacular astrophysical phenomena, but are also fundamental in the evolution of galaxies (Fabian, 2012). As matter accretes onto a supermassive black hole, up to 10% of its rest mass energy is released in the form of radiation, winds, and relativistic jets. This energy can couple to the surrounding medium and influence the thermal and dynamical state of the interstellar medium (ISM) and the intracluster medium. This process, known as AGN feedback, regulates both black hole growth and galaxy evolution.

The need for AGN feedback is evident when comparing the energy budget of a galaxy to that of its central black hole. The binding energy of a galactic bulge with mass  $M_{\text{gal}}$  and velocity dispersion  $\sigma$  is approximately  $E_{\text{gal}} \sim M_{\text{gal}}\sigma^2$ . By contrast, the energy released during the growth of a black hole of mass  $M_{\text{BH}} \sim 10^{-3}M_{\text{gal}}$  is  $E_{\text{BH}} \sim 0.1M_{\text{BH}}c^2$ . For typical galaxies,  $E_{\text{BH}}$  exceeds  $E_{\text{gal}}$  by over an order of magnitude. Even if only a small fraction of this energy is transferred to the surrounding gas, it is sufficient to heat, expel, or redistribute the ISM. This naturally explains the observed correlations between black hole mass and bulge properties (such as the  $M_{\text{BH}} - \sigma$  relation), see Ferrarese and Merritt (2000).

Furthermore, without a regulating mechanism, massive galaxies at the centres of clusters would form stars at unsustainably high rates due to radiative cooling of the hot ICM. Observations show that this is not the case: star formation is suppressed, and the gas remains hot. AGN feedback provides the missing heating source that offsets cooling (McNamara and Nulsen, 2007).

Two principal modes of AGN feedback have been identified:

**Radiative or “quasar” mode** The radiative mode occurs when the black hole accretes efficiently, close to its Eddington limit<sup>1</sup>. This is most relevant at high redshift ( $z \sim 2 - 3$ ), when galaxies were gas-rich and quasar activity peaked. The intense radiation field exerts pressure on dusty gas, and powerful winds with velocities of several thousand km/s are launched from the accretion disk (King and Pounds, 2003). These winds sweep out large reservoirs of cold gas, shutting down star formation.

Evidence for this mode comes from broad absorption line quasars, showing outflows at tens of thousands of km/s (Ganguly and Brotherton, 2007), ultraluminous infrared galaxies with massive molecular outflows (Cicone et al., 2014) and systems such as Mrk 231, where outflow rates exceed the star formation rate, indicating that the AGN dominates the feedback (Rupke and Veilleux, 2011).

The radiative mode is thought to be responsible for establishing the black hole–galaxy co-evolution relation and for transforming star-forming “blue cloud” galaxies into passive “red sequence” systems (Hopkins and Hernquist, 2006).

---

<sup>1</sup>The Eddington limit is the maximum luminosity at which the outward radiation pressure balances the inward gravitational pull on the accreting material. It is given by  $L_{\text{Edd}} = \frac{4\pi GM_{\text{BH}}m_p c}{\sigma_T} \approx 1.3 \times 10^{38} \left(\frac{M_{\text{BH}}}{M_{\odot}}\right) \text{ erg s}^{-1}$ , where  $M_{\text{BH}}$  is the black hole mass,  $m_p$  the proton mass, and  $\sigma_T$  the Thomson cross-section.

**Kinetic or “radio” mode** The kinetic mode dominates in the present-day Universe, especially in massive galaxies at the centres of groups and clusters. Here the black hole accretes at a relatively low Eddington fraction, but produces powerful relativistic jets. These jets inflate cavities or bubbles in the surrounding ICM, which are directly observed as depressions in X-ray images coincident with radio lobes.

The inflated bubbles rise buoyantly, displacing cold gas while distributing energy through shocks, sound waves, and turbulence (Fabian, 2003). The mechanical power of the jets, inferred from the work done to inflate the bubbles, is sufficient to balance or even exceed the radiative cooling losses of the ICM (Rafferty et al., 2006).

This feedback loop, often referred to as “maintenance mode”, prevents runaway cooling and suppresses star formation in the brightest cluster galaxies. It explains why these galaxies are massive, old, and red, rather than forming stars at rates of hundreds of solar masses per year.

**Giant radio galaxy mode** A further, less well understood regime involves giant radio galaxies whose lobes can extend over megaparsecs. The mechanical energy involved in such outbursts can approach the binding energy of the gas in groups and small clusters, suggesting a devastating impact on their environments.

The observational evidences regarding AGN feedback are now well established, such as X-ray cavities and bubbles, strong absorption lines, quenching of star formation in massive galaxies, especially at high redshift, and Faraday rotation study, to infer the properties of magnetic fields in cluster cores.

AGN feedback is self-regulating: when gas cools and accretes, the black hole powers up, producing more energy and halting the inflow. Once heating dominates, accretion is lowered, and the AGN fades, allowing cooling to resume. This cycle maintains the observed rough balance between heating and cooling in cluster cores over billions of years.

Simulations confirm that such feedback can reproduce many observed galaxy properties, including the cut-off at the bright end of the luminosity function and the bimodal colour distribution of galaxies (Springel et al., 2005).

AGN feedback has big consequences for cosmology and structure formation. It regulates the growth of massive galaxies, prevents excessive cooling flows in clusters, and sets the conditions for galaxy scaling relations. Moreover, it links processes occurring on sub-parsec scales near the black hole to phenomena extending over hundreds of kiloparsecs.

## PKS 2316-423 and its Cluster Environment

This section provides an overview of the target source, presenting its fundamental characteristics and reviewing the existing observational evidence that forms the basis for the analysis presented in this work.

This object is an AGN mostly known as PKS 2316-423 after its cataloguing in the PKS90 catalogue of radio sources (Wright and Otrupcek, 1990), performed using the Parkes Radio Telescope. The coordinates of this object in the J2000 coordinate system are RA 23h 19m 06s DEC  $-42^{\circ} 06' 40''$ , with a redshift of  $z=0.055$ , obtained spectroscopically from the host galaxy (Zabludoff and Mulchaey, 1998).

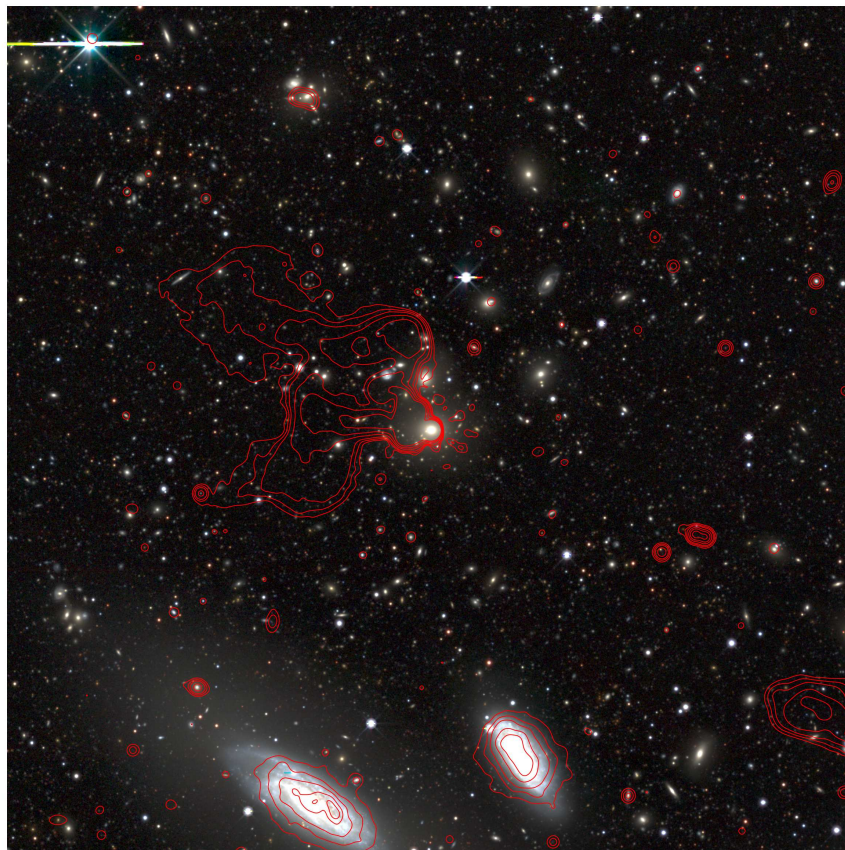


**Figure 7.** Image of the Abell S1111 field from the DESI (Dark Energy Spectroscopic Instrument) Legacy Survey. The foreground galaxies NGC 7599 and NGC 7590 are visible in the bottom. Red contours correspond to the MeerKAT image centred at 1.25 GHz, with a synthesized beam of  $7.6'' \times 7.2''$ .

PKS 2316-423 is associated with the BCG of Abell S1111, also known as Sérsic 159-02, which is of Abell richness class 0, the smallest one. This is visible in figure 7, where 1.25 GHz MeerKAT contours (discussed in detail in Section 7) are overlaid on top of the DESI

Legacy Survey image of the cluster.

The host galaxy is identified with MCG-07-47-031, an Early Type with a stellar mass of  $M \approx 3.3 \times 10^{11} M_{\odot}$  with little to none star formation occurring. Its optical spectrum is presented in the analysis of Crawford and Fabian (1994), showing a domination from the host galaxy, also confirmed by the spectrum present in the 6dF Galaxy Survey (6dFGS) (Jones et al., 2004) and reported in Figure 8.

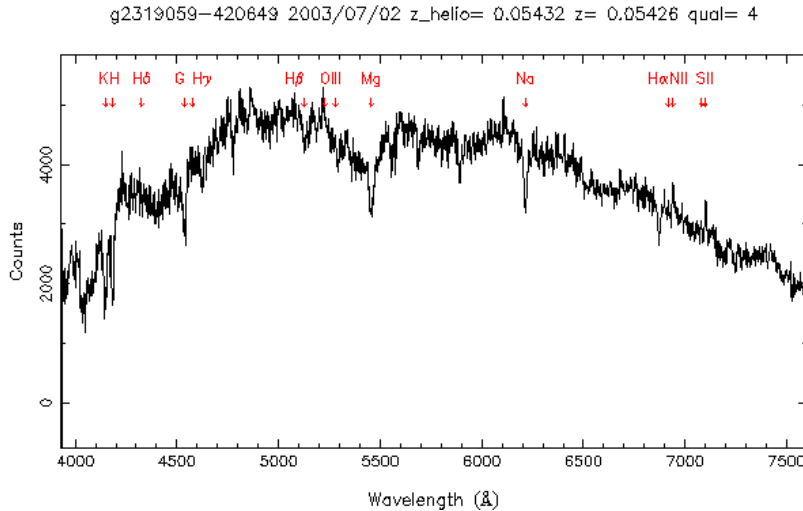


**Figure 8.** The image shows the optical spectrum obtained from the 6dFGS galaxy survey from 3900 Å to 7600 Å.

Other useful parameters derived in the optical band come from the work by Wen and Han (2024), that estimate a mass of the cluster  $m_{500}^2 \approx 7.7 \times 10^{13} M_{\odot}$ , on the lower end of the typical masses found in galaxy cluster, consistent with the classification of Abell, which is instead based on the number of galaxies nearby.

This source was classified as a BL Lac after the detection of its X-ray and Gamma-ray emission, obtained from observations with the Einstein observatory (Maccacaro et al., 1981) and Fermi Large Area Telescope Fourth Source Catalog (4FGL) (Abdollahi et al., 2020). A more recent X-ray measurement with XMM-Newton shows a spectrum, presented in Figure 9, perfectly compatible with a single power law, proving the non-thermal origin of this emission Glowacki et al. (2017).

This object has been observed numerous times in different radio surveys. An extended radio structure was detected by Jones and McAdam (1992) using the Molonglo observatory Synthesis Telescope (MOST) at 843 MHz with a resolution of 44", obtaining the image shown in Figure 10.

Later measurements with the Parkes radio telescope from 480 MHz to 8.4 GHz seem to prove the non-thermal origin of the radiation also in the radio regime, displaying a power law behaviour (see Section 7.2.2). These observations come from a single dish survey, therefore are not able to separate the extended emission from the core contamination due to the large size of the beam.

---

<sup>2</sup>Defined as the total mass enclosed within the radius  $R_{500}$ , where the mean density is 500 times the critical density of the Universe at the cluster redshift.

A spectro-polarimetric study, performed using the Giant Metrewave Radio Telescope at 610 MHz by Farnes et al. (2014), detected the object both in total intensity and polarization, but the resolution and sensitivity were not enough to perform a multi-frequency analysis.

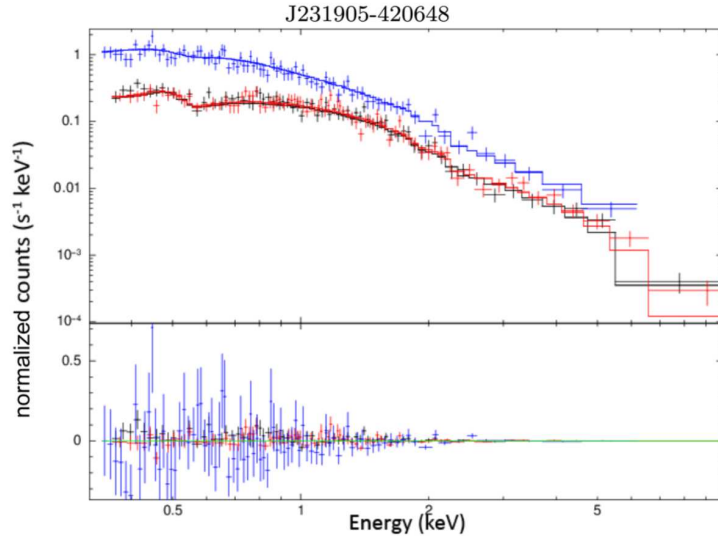


**Figure 9.** The image shows the X-ray spectrum of the source obtained with XMM-Newton, in particular the top panel reports the normalized counts for the EMOS1, EMOS2 and EPN detectors, in black, red and blue, respectively, while the bottom panel shows the residuals. Credit Glowacki et al. (2017).

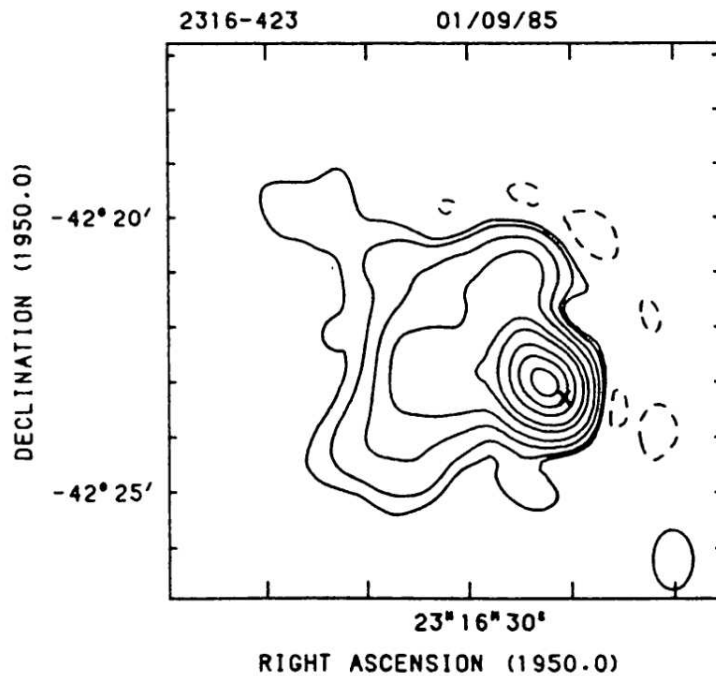


**Figure 10.** The image shows the extended radio emission at 843 MHz obtained with MOST, with a resolution of  $44''$  and contours starting at  $0.54 \text{ Jy/beam}$ . Credit Jones and McAdam (1992)

More recent measurements include the ones from the Rapid ASKAP Continuum Survey (RACS) (McConnell et al., 2020) using the ASKAP interferometer at frequencies of 888, 1367 and 1655 MHz, where the source is detected in total intensity. The images, reported in Figure 11, show more extended emission than the one detected in previous studies, but the automatized data reduction creates many artefacts due to the presence of the very bright core and limits the reachable dynamic range.

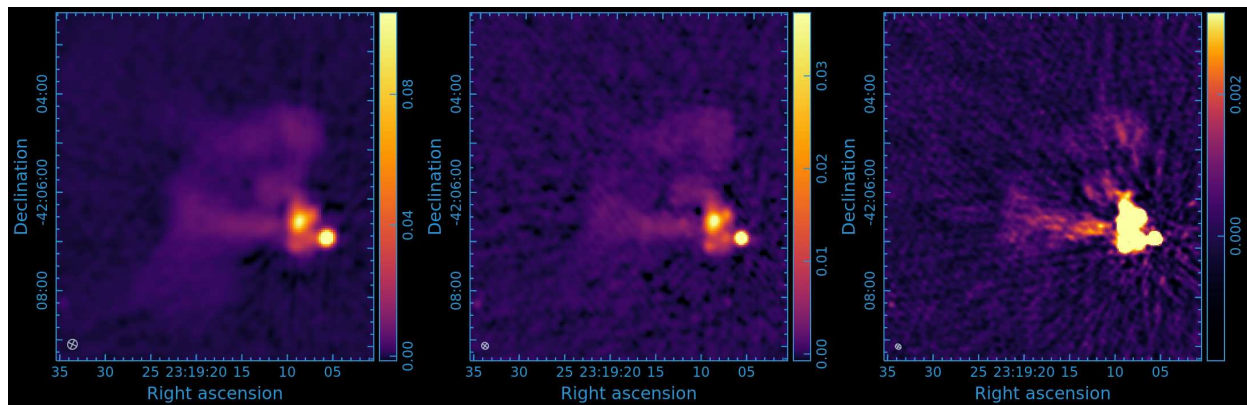


**Figure 11.** The figure shows from left to right total intensity RACS image at 888, 1367, 1655 MHz, with a circular beam size of 12, 9, 7 arcseconds and all with a pixel spacing of 1.5, 2 and 2.5 arcsec/pixel respectively.

The lack of high-sensitivity multi-frequency radio observations has so far prevented a detailed spectral analysis of the synchrotron emission, which is crucial for constraining the source’s life cycle, its possible interactions with the intracluster medium, and for achieving a comprehensive characterization of the unexpectedly extended emission from this BL Lac object. In this work, these aspects are addressed through deep MeerKAT observations, complemented by a polarimetric study that will be used to characterize the ICM.

Throughout this work we assume a flat  $\Lambda$ CDM cosmology with  $H_0 = 70 \text{ km s}^{-1} \text{ Mpc}^{-1}$ ,  $\Omega_m = 0.3$ , and  $\Omega_\Lambda = 0.7$ , therefore, using the value of  $z=0.055$  as a distance for the source, one arcminute correspond to 64.14 kpc.

## Radio Astronomical Background

Radio astronomy is the study of natural radio emission from celestial sources. The radio band is very broad, spanning between 10 MHz and 1 THz, at the lower frequencies of the electromagnetic spectrum. Radio wavelengths are much longer than atmospheric dust grains and the Sun is not an overwhelmingly bright radio source, so the radio sky is always dark and many radio observations can be made day or night.

Few astronomical radio sources are obscured because radio waves can penetrate interstellar dust clouds and Compton-thick layers of neutral gas.

Nearly everything emits radio waves at some level, via a wide variety of emission mechanisms. These can be broadly divided into thermal and non-thermal mechanisms. Thermal emission is produced when the emitting particles are in local thermodynamic equilibrium (LTE), otherwise, the emission is classified as non-thermal.

Thermal processes include blackbody radiation, by which all matter with a temperature above absolute zero emits across the electromagnetic spectrum, including the radio band (though generally weak at these long wavelengths). Another important mechanism is free-free emission (Bremsstrahlung), produced when free electrons are accelerated in the Coulomb field of ions, as occurs in H II regions and hot plasma. In addition, thermal dust emission from cold dust grains (10-100 K) radiates primarily in the millimeter and submillimeter regimes.

Non-thermal processes, in contrast, dominate in many energetic astrophysical environments. The most prominent is synchrotron radiation, generated by relativistic electrons spiralling around magnetic field lines, which is the main source of radio emission in AGNs, radio galaxies, pulsars, and supernova remnants. Related to this, cyclotron or gyroresonance radiation is produced by non-relativistic or mildly relativistic electrons in magnetic fields, and is particularly relevant in planetary magnetospheres and solar radio bursts. Finally, maser emission, arising from stimulated emission in molecules such as OH, H<sub>2</sub>O, SiO, and CH<sub>3</sub>OH, produces extremely bright and narrow-band spectral lines, especially in star-forming regions and around evolved stars.

Section 5.1 presents an overview of synchrotron emission, the dominant mechanism responsible for the radiation detected from the sources analyzed in this thesis. Section 5.2 introduces the Faraday effect, which constitutes the focus of the analysis in Section 7.3.1. Finally, Sections 5.3 and 5.4 provide an overview of the fundamental parameters of radio astronomy and of the radio telescopes employed in these studies.

### 5.1 Synchrotron Radiation

When a charged particle is accelerated, it emits electromagnetic radiation with power specified by Larmor's formula:

$$P = \frac{2q^2 \dot{v}^2}{3c^3}. \quad (1)$$

When the cause for this acceleration is a magnetic field, the phenomena takes the name of *magnetobremstrahlung*, the German term for "magnetic braking radiation". The lightest charged particles (electrons, and positrons if present) are accelerated much more than protons and other ions due to the lower mass, so electrons and positrons account for virtually all of the observed radiation. The character of magnetobremstrahlung depends on the electron energies, and different regimes are distinguished as follows.

*Gyro radiation* arises from electrons with velocities much smaller than the speed of light ( $v \ll c$ ). *Cyclotron radiation* is emitted by mildly relativistic electrons with kinetic energies comparable to their rest mass energy ( $E_{\text{kin}} \sim m_e c^2$ ). Finally, *synchrotron radiation* is produced by ultrarelativistic electrons with kinetic energies much greater than their rest mass energy ( $E_{\text{kin}} \gg m_e c^2$ ).

Synchrotron radiation is ubiquitous in astronomy. It accounts for most of the radio emission from Active Galactic Nuclei, powered by accretion onto supermassive black holes in galaxies and quasars, and it dominates the radio continuum emission from star-forming galaxies, including the Milky Way, at frequencies below  $\nu \sim 30$  GHz. Relativistic electrons in nearly all synchrotron sources follow power-law energy distributions, which means they are not in local thermodynamic equilibrium (LTE). For this reason, synchrotron sources are often called "nonthermal" sources. However, a synchrotron source with a relativistic Maxwellian electron distribution would be a thermal source, so "synchrotron" and "nonthermal" are not strictly synonymous.

The magnetic force  $\vec{F}$  exerted on a charged particle by a magnetic field  $\vec{B}$  is given by

$$\vec{F} = \frac{q}{c} (\vec{v} \times \vec{B}). \quad (2)$$

Where  $\vec{v}$  is the velocity of the particle,  $q$  its charge,  $c$  the light speed and  $\vec{B}$  the magnetic field vector. This means that the force applied to the charge particle is perpendicular to its velocity, making the particles spirals around magnetic field lines, as shown in Figure 12.

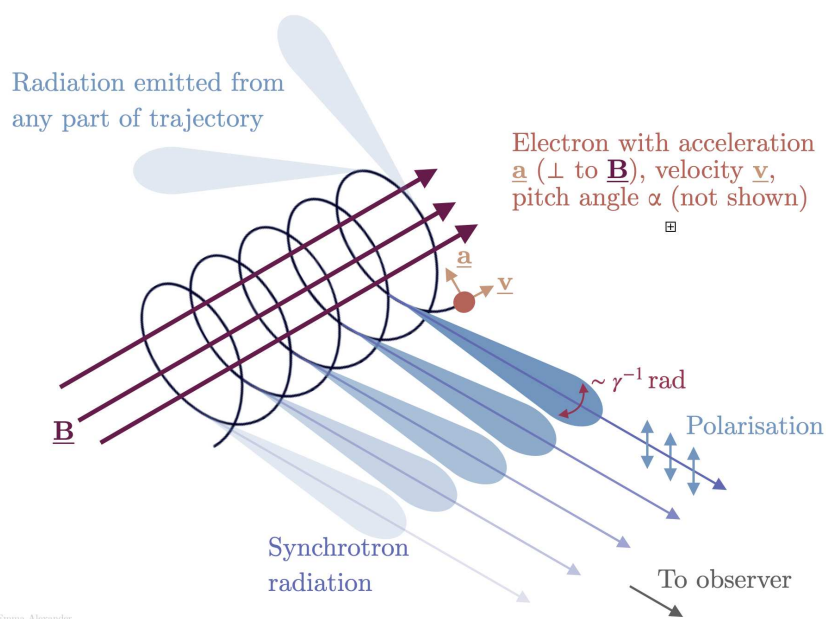


**Figure 12.** The image shows the mechanism at the base of synchrotron radiation.

The synchrotron power radiated by a single electron depends on physical constants, the square of the electron kinetic energy (via  $\gamma^2$ ), the magnetic energy density  $U_B$ , and the pitch angle  $\alpha$ :

$$P = 2\sigma_T \beta^2 \gamma^2 c U_B \sin^2 \alpha. \quad (3)$$

Where  $\sigma_T$  is the Thompson scattering cross section and  $\beta$  is the Lorentz factor.

Relativistic electrons in radio sources can have lifetimes of thousands to millions of years before losing their ultrarelativistic energies via synchrotron radiation or other processes. During their lifetimes, repeated scattering by magnetic field fluctuations and charged particles tends to randomize their pitch angles, leading to an isotropic distribution. In this case, the average synchrotron power per electron becomes

$$P = \frac{4}{3} \sigma_T \beta^2 \gamma^2 c U_B. \quad (4)$$

For a homogeneous and isotropic population of electrons with a power-law energy distribution, such that the particle density between  $\epsilon$  and  $\epsilon + d\epsilon$  is

$$N(\epsilon) d\epsilon = N_0 \epsilon^{-\delta} d\epsilon, \quad (5)$$

the total intensity spectrum in regions that are optically thin to their own radiation varies as

$$S(\nu) \propto \nu^\alpha, \quad (6)$$

where the spectral index  $\alpha$  is related to the electron energy index  $\delta$  by

$$\alpha = -\frac{\delta - 1}{2}. \quad (7)$$

When a single electron produces an electromagnetic wave, its electric field is intrinsically polarized in the direction perpendicular to the magnetic field along which the electron spirals.

In realistic astrophysical sources, however, the observed radiation results from the superposition of photons emitted by a large population of electrons with different energies, phases, and pitch angles. If the magnetic fields along the line of sight are randomly oriented, the resulting emission appears unpolarized. In contrast, an ordered magnetic field yields synchrotron emission with a significant degree of linear polarization, up to a theoretical maximum of

$$\Pi_{\max} = \frac{|\alpha| + 1}{|\alpha| + 5/3}, \quad (8)$$

where  $\alpha$  is the synchrotron spectral index (Rybicki and Lightman, 1979). In practice, turbulence and field irregularities reduce this ideal value.

## 5.2 Faraday Rotation and depolarization

A linearly polarized electromagnetic wave propagating through a magnetized plasma undergoes *Faraday rotation*. The wave can be decomposed into right- and left-handed circularly polarized modes, which propagate at different velocities. This difference leads to a progressive rotation of the plane of polarization. Using the dispersion relation, the refractive indices for the two modes are:

$$n_{L,R} = \left(1 - \frac{\omega_P^2}{\omega^2 \pm \omega \Omega_e}\right)^{1/2}, \quad (9)$$

where  $\omega_P = \left(\frac{4\pi n_e e^2}{m_e}\right)^{1/2}$  is the plasma frequency and  $\Omega_e = \frac{eB}{m_e c}$  is the electron cyclotron frequency. For typical intracluster medium conditions ( $B \sim 1 \mu\text{G}$ ,  $n_e \sim 10^{-3} \text{cm}^{-3}$ ), radio frequencies satisfy  $\omega \gg \Omega_e$ , allowing Eq. 9 to be approximated as

$$n_{L,R} \approx 1 - \frac{1}{2} \frac{\omega_P^2}{\omega^2 \pm \omega \Omega_e}. \quad (10)$$

The resulting time delay between the two modes over a path  $dl$  is

$$\Delta t = \frac{\omega_P^2 \Omega_e dl}{c \omega^3} = \frac{4\pi e^3}{\omega^2 m_e^2 c^2} n_e B dl, \quad (11)$$

leading to a phase difference  $\Delta\phi = \omega \Delta t$ . Over a total path length  $L$ , the intrinsic polarization angle  $\Psi_{\text{Int}}$  is rotated by

$$\Psi_{\text{Obs}}(\lambda) = \Psi_{\text{Int}} + \frac{e^3 \lambda^2}{2\pi m_e^2 c^4} \int_0^L n_e(l) B_{\parallel}(l) dl, \quad (12)$$

where  $B_{\parallel}(l)$  is the line-of-sight magnetic field. The integral term defines the *Rotation Measure* (RM), giving the standard expression

$$\Psi_{\text{Obs}}(\lambda) = \Psi_{\text{Int}} + \lambda^2 RM, \quad (13)$$

with

$$RM = \frac{e^3}{2\pi m_e^2 c^4} \int_0^L n_e(l) B_{\parallel}(l) dl. \quad (14)$$

In practical astrophysical units,

$$RM \left[ \frac{\text{rad}}{\text{m}^2} \right] = 812 \int_0^L n_e [\text{cm}^{-3}] B_{\parallel} [\mu\text{G}] dl [\text{kpc}]. \quad (15)$$

By convention, RM is positive if the magnetic field points towards the observer and negative if directed away. The polarization angle  $\Psi_{\text{Obs}}$  is observable, so RM can be determined by fitting the linear  $\Psi-\lambda^2$  relation across multiple frequencies, which also removes the  $\Psi \pm n\pi$  ambiguity. This linear model is valid when the source lies behind a thin Faraday screen; more complex cases are discussed in Section 7.3.1.

Faraday rotation can also cause depolarization. *Beam depolarization* arises when unresolved fluctuations in electron density or magnetic field strength produce RM variations within the observing beam, averaging out the signal. *Bandwidth depolarization* occurs when significant rotation of the polarization angle takes place across the observing bandwidth, reducing the net polarization after averaging. *Internal depolarization*, in contrast, is intrinsic to extended (along the line of sight) sources: radiation emitted at different depths experiences different amounts of Faraday rotation, leading to partial cancellation in the summed emission.

Distinguishing between external and internal depolarization requires high-resolution, multi-frequency polarization data. The key difference is that internal depolarization correlates with the absolute value of RM, so regions with small RM should show little depolarization. External depolarization, however, depends on unresolved RM gradients in the foreground medium and is therefore linked to the strength of the RM gradient rather than its magnitude.

## 5.3 Fundamental Quantities in Radio Astronomy

Astronomers study an astronomical source by measuring the strength of its radiation as a function of direction on the sky (by mapping or imaging) and frequency (spectroscopy), plus other quantities (time, polarization) to be considered later. Clear and quantitative definitions are needed to describe the strength of radiation and how it varies with direction, frequency, and distance between the source and the observer.

We distinguish between the brightness or intensity of a source's radiation, which does not depend on distance, and the apparent flux, which does.

The total brightness is contributed by photons of all frequencies. The brightness per unit frequency is called the *specific intensity* (also *spectral intensity* or *spectral brightness*). The notation for specific intensity is  $I_\nu$ , where the subscript  $\nu$  is used to indicate per unit frequency. In the ray-optics approximation, specific intensity can be defined quantitatively in terms of:

- $d\sigma$  = an infinitesimal surface area (e.g., of a detector);
- $\theta$  = the angle between a "ray" of radiation and the normal to the surface;
- $d\Omega$  = an infinitesimal solid angle measured from the observer's location.

The surface containing  $d\sigma$  can be any surface, real or imaginary; that is, it could be the physical surface of the detector, the source, or an imaginary surface anywhere along the ray. If an energy  $dE$  from within the solid angle  $d\Omega$  flows through the projected area  $\cos\theta d\sigma$  in time  $dt$  and in a narrow frequency band of width  $d\nu$ , then

$$dE = I_\nu \cos\theta d\sigma d\Omega dt d\nu. \quad (16)$$

Power is defined as the flow of energy per unit time, so the corresponding power  $dP$  is

$$dP = \frac{dE}{dt} = I_\nu \cos\theta d\sigma d\Omega d\nu, \quad (17)$$

with units of (Watts) =  $(\text{m}^2 \text{sr Hz})^{-1}$ . Thus, the quantitative definition of specific intensity or spectral brightness is

$$I_\nu \equiv \frac{dP}{(\cos\theta d\sigma) d\nu d\Omega}, \quad (18)$$

and the SI units of  $I_\nu$  are  $\text{W m}^{-2} \text{Hz}^{-1} \text{sr}^{-1}$ .

If a source is *discrete*, meaning that it subtends a well-defined solid angle, the spectral power received by a detector of unit projected area is called the *flux density*  $S_\nu$  of the source. Equation 18 implies

$$dP = I_\nu \cos\theta d\Omega, \quad (19)$$

so integrating over the solid angle subtended by the source yields

$$S_\nu \equiv \int_{\text{source}} I_\nu(\theta, \phi) \cos\theta d\Omega. \quad (20)$$

The MKS units of flux density,  $\text{W m}^{-2} \text{Hz}^{-1}$ , are much too large for practical astronomical use. Astronomers therefore adopt a smaller unit, the *Jansky*, defined as

$$1 \text{ Jansky} = 1 \text{ Jy} \equiv 10^{-26} \text{ W m}^{-2} \text{ Hz}^{-1}. \quad (21)$$

The flux density of a source also depends on the distance between the source and the observer. The *total flux* (or simply *flux*)  $S$  from a source is the integral of the flux density over frequency:

$$S \equiv \int_0^\infty S_\nu d\nu. \quad (22)$$

Its dimensions are power divided by area, and its MKS units are  $\text{W m}^{-2}$ . The *spectral luminosity*  $L_\nu$  of a source is defined as the total power per unit bandwidth radiated at frequency  $\nu$ , with MKS units of  $\text{W Hz}^{-1}$ . Since the area of a sphere of radius  $d$  is  $4\pi d^2$ , the relation between the spectral luminosity and the flux density of an isotropic source radiating in free space is

$$L_\nu = 4\pi d^2 S_\nu, \quad (23)$$

where the distance  $d$  between the source and the observer is assumed to be much larger than the size of the source itself.

Another important quantity adopted by astronomers is the *brightness temperature*  $T_b$ . It is defined as the temperature that a blackbody would have in order to produce the same specific intensity  $I_\nu$  at a given frequency. Using the Rayleigh–Jeans approximation to the Planck law, valid in the radio regime ( $h\nu \ll k_B T$ ), the specific intensity of blackbody radiation can be written as

$$I_\nu = \frac{2k_B T_b \nu^2}{c^2}, \quad (24)$$

where  $k_B$  is the Boltzmann constant. Hence, for any observed source with specific intensity  $I_\nu$ , the brightness temperature is

$$T_b = \frac{c^2}{2k_B \nu^2} I_\nu. \quad (25)$$

Although  $T_b$  does not represent a true thermodynamic temperature in most astrophysical contexts, it provides a convenient way to characterize the intensity of radio sources. For example, thermal emitters such as H II regions have brightness temperatures comparable to their physical electron temperatures ( $\sim 10^4$  K), while non-thermal synchrotron sources, such as active galactic nuclei, can exhibit brightness temperatures that formally exceed  $10^{12}$  K, indicating emission processes far from thermal equilibrium.

## 5.4 Radio Telescopes

Radio telescopes are designed to detect and measure faint radio signals from astrophysical sources. They do not measure the intrinsic physical quantities of radiation directly (such as  $I_\nu$  or  $S_\nu$ ), but rather instrumental quantities that must be calibrated and converted into source properties. Two main observational approaches are employed: single-dish observations and radio interferometry.

### 5.4.1 Single dish

A single-dish radio telescope consists of a parabolic reflector that collects incoming radio waves and focuses them onto a receiver at the focal point, as shown in the schematics present in Figure 13 (Bolli et al., 2015).

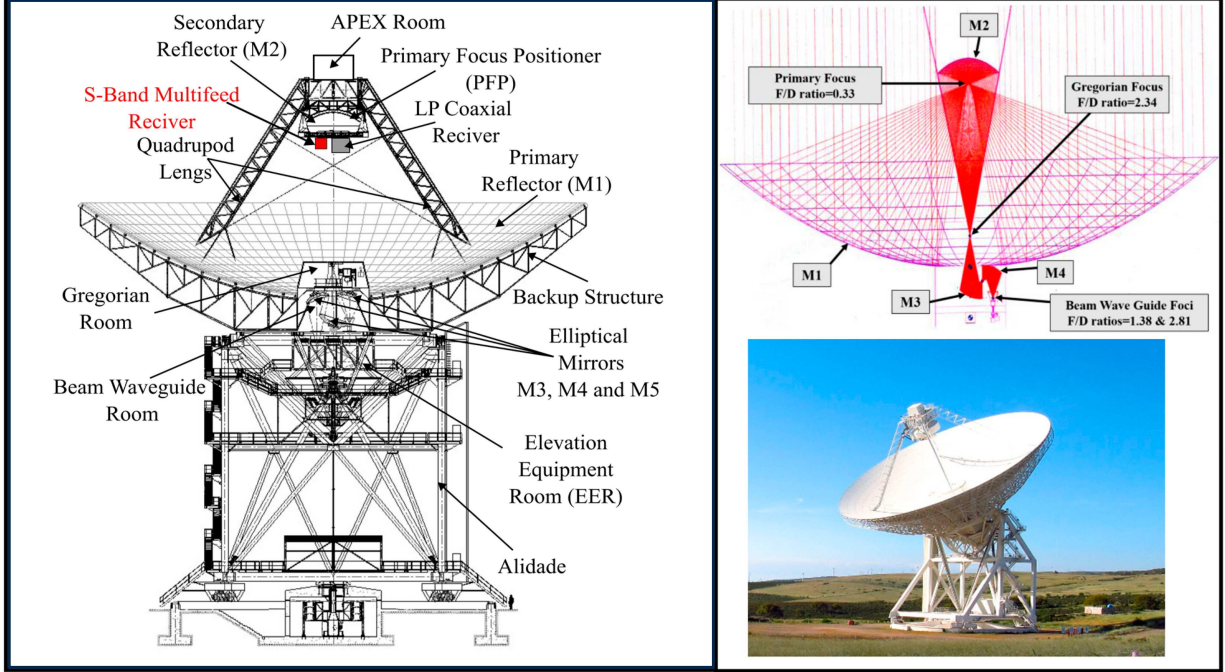


**Figure 13.** The Sardinia Radio Telescope (SRT), a 64-meter single-dish radio telescope. *Left:* Technical schematic of the telescope structure. *Top right:* Optical ray-tracing of the Gregorian and beam waveguide configurations, illustrating the multiple foci used for different receiver systems. *Bottom right:* Photograph of the SRT in operation. The telescope operates from 0.3 to 26.5 GHz and supports multiple observing modes including single-dish continuum, spectroscopy, and VLBI.

The response of the telescope is quantified through several key parameters.

**Beamwidth and Beam Solid Angle** The angular resolution of a dish of diameter  $D$  observing at wavelength  $\lambda$  is approximately

$$\theta_{\text{FWHM}} \simeq 1.22 \frac{\lambda}{D}, \quad (26)$$

where  $\theta_{\text{FWHM}}$  is the full width at half maximum (FWHM) of the main lobe of the antenna pattern. The beam solid angle is defined as

$$\Omega_A = \int_{4\pi} P_n(\theta, \phi) d\Omega, \quad (27)$$

where  $P_n(\theta, \phi)$  is the normalized antenna power pattern. The beam efficiency is given by the ratio of the main lobe solid angle to the total beam solid angle,

$$\eta_B = \frac{\Omega_{\text{MB}}}{\Omega_A}, \quad (28)$$

which quantifies how much of the collected power comes from the main lobe compared to sidelobes.

**Effective Area and Gain** The effective collecting area  $A_{\text{eff}}$  of the dish is related to its physical (geometric) area  $A_{\text{geom}}$  by the aperture efficiency  $\eta_A$ ,

$$A_{\text{eff}} = \eta_A A_{\text{geom}} = \eta_A \frac{\pi D^2}{4}. \quad (29)$$

The antenna gain  $G$  is related to  $A_{\text{eff}}$  through

$$G = \frac{4\pi A_{\text{eff}}}{\lambda^2}. \quad (30)$$

**Antenna Temperature and Flux Density** The power collected by the antenna can be expressed in terms of the antenna temperature  $T_A$ , which is related to the source flux density  $S_\nu$  by

$$S_\nu = \frac{2k_B}{A_{\text{eff}}} T_A. \quad (31)$$

**System Temperature and Sensitivity** The total system temperature is the sum of contributions from different noise sources:

$$T_{\text{sys}} = T_{\text{rec}} + T_{\text{sky}} + T_{\text{spill}} + T_{\text{cmb}} + \dots \quad (32)$$

where  $T_{\text{rec}}$  is the receiver temperature,  $T_{\text{sky}}$  is atmospheric emission,  $T_{\text{spill}}$  accounts for spillover from the ground, and  $T_{\text{cmb}} \simeq 2.73$  K is the cosmic microwave background temperature.

The sensitivity of a single-dish telescope is limited by thermal noise, given by the radiometer equation:

$$\Delta T = \frac{T_{\text{sys}}}{\sqrt{\Delta\nu t}}, \quad (33)$$

where  $\Delta\nu$  is the observing bandwidth and  $t$  the integration time.

**Applications** Single-dish telescopes are particularly powerful for measuring total power and diffuse large-scale structures, such as Galactic synchrotron emission, pulsar flux densities, or the Sunyaev–Zel’dovich effect in galaxy clusters. However, their angular resolution is limited by the dish size, which motivates the use of interferometry for high-resolution imaging.

## 5.4.2 Radio Interferometry

The angular resolution of a single-dish telescope is limited by its physical diameter  $D$ , with  $\theta \sim \lambda/D$ . To achieve higher resolution at radio wavelengths, which are typically much longer than optical ones, it is impractical to build extremely large single reflectors. This challenge is overcome by *radio interferometry*, which combines signals from multiple antennas separated by large distances, effectively synthesizing a telescope with an aperture equal to the maximum separation between elements.

**Principle of Interferometry** The fundamental observable of an interferometer is the *visibility function*  $V(u, v)$ , obtained by cross-correlating the voltages measured by a pair of antennas separated by a baseline  $\mathbf{B}$ . Expressed in units of the observing wavelength, the baseline projects onto coordinates  $(u, v)$  in the so-called *uv-plane*, with an example visible in Figure 14. The van Cittert–Zernike theorem states that the visibility function is the Fourier transform of the sky brightness distribution  $I(l, m)$ :

$$V(u, v) = \iint I(l, m) e^{-2\pi i(ul+vm)} dl dm, \quad (34)$$

where  $(l, m)$  are the direction cosines relative to the pointing center.

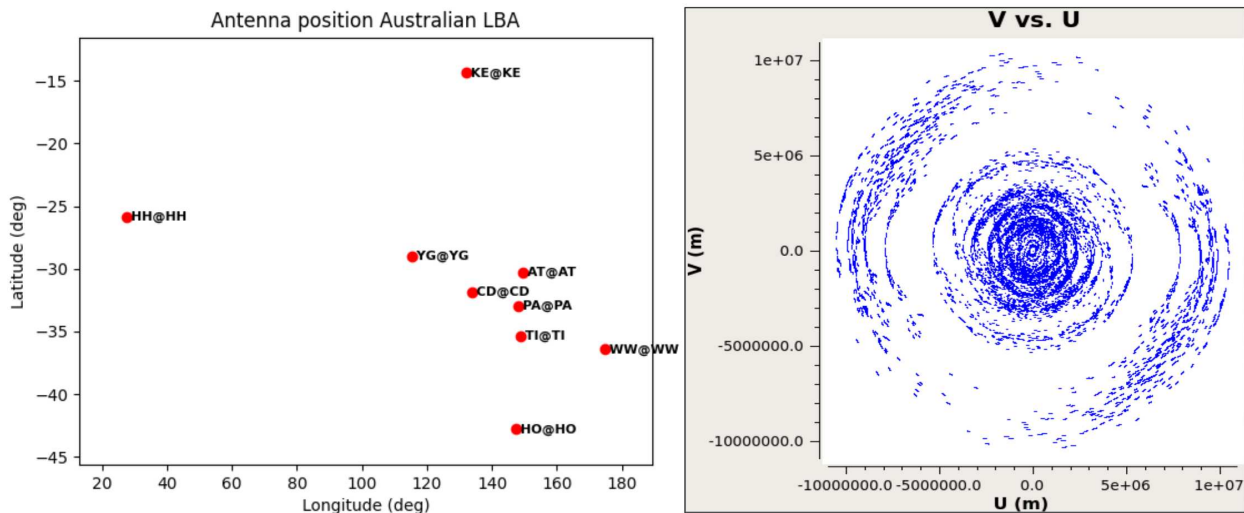


**Figure 14.** *Left:* Example of antenna positions for Australian Very Large Baseline Array, where the labels indicate the code for each antenna name. *Right:*  $uv$ -coverage obtained from those antennas.

**$uv$ -Coverage and Synthesized Beam** Each antenna pair, samples one Fourier component of the sky per integration time. As the Earth rotates, the projected baselines change, gradually filling the  $uv$ -plane. The more completely this plane is sampled, the higher the fidelity of the reconstructed image. The inverse Fourier transform of the sampled visibilities produces the *dirty image*, which is the convolution of the true sky brightness with the *dirty beam* (or point-spread function), defined as

$$B(l, m) = \iint S(u, v) e^{-2\pi i(ul+vm)} du dv, \quad (35)$$

where  $S(u, v)$  is the sampling function in the  $uv$ -plane.

**Angular Resolution** The resolution of an interferometer is set by the maximum projected baseline  $B_{\max}$ ,

$$\theta \sim \frac{\lambda}{B_{\max}}, \quad (36)$$

which can be orders of magnitude smaller than that of any single dish. For example, Very Long Baseline Interferometry achieves milliarcsecond resolution by combining antennas thousands of kilometers apart. However, interferometers are insensitive to emission on angular scales larger than those sampled by the shortest baselines, leading to the *missing short spacings* problem.

**Advantages and Limitations** Interferometers provide high-resolution imaging of radio sources, enabling studies of compact structures such as AGN jets, pulsars, and star-forming regions with extreme details. However, they suffer from incomplete sampling of spatial frequencies, requiring deconvolution techniques to reconstruct images. They also lack sensitivity to large-scale diffuse emission, which is instead best observed with single-dish telescopes. The two techniques are therefore complementary, and in practice are often combined to achieve both high angular resolution and sensitivity to extended structures.

## Observations and data reduction

This section provides a summary of what has been done with the MeerKAT dataset, Section 6.1 presents an overview of the configuration that were used during the observations, while Section 6.2 explains how the dataset has been reduced.

### 6.1 Observations

The MeerKAT data used in this work consist of two Measurement Sets (MS), corresponding to separate observing sessions (I.D. MKT-22120, P.I. Francesca Loi). The first observation was conducted on 10 June 2023, with a duration of 4 hours and 45 minutes, alternating between the target and calibrators. The second observation followed a nearly identical strategy on 5 August 2023. Both sessions employed 63 MeerKAT antennas in L-band, covering a frequency range of 856–1711 MHz, divided into 32k channels, leading to a spectral resolution of 26 kHz per channel. For processing, only the 900–1600 MHz band was used in order to avoid the bandpass roll-off, where the receiver response is no longer linear. The channels were also reduced reaching a spectral resolution of  $\sim 209$  kHz, which is sufficient for our spectropolarimetric analysis.

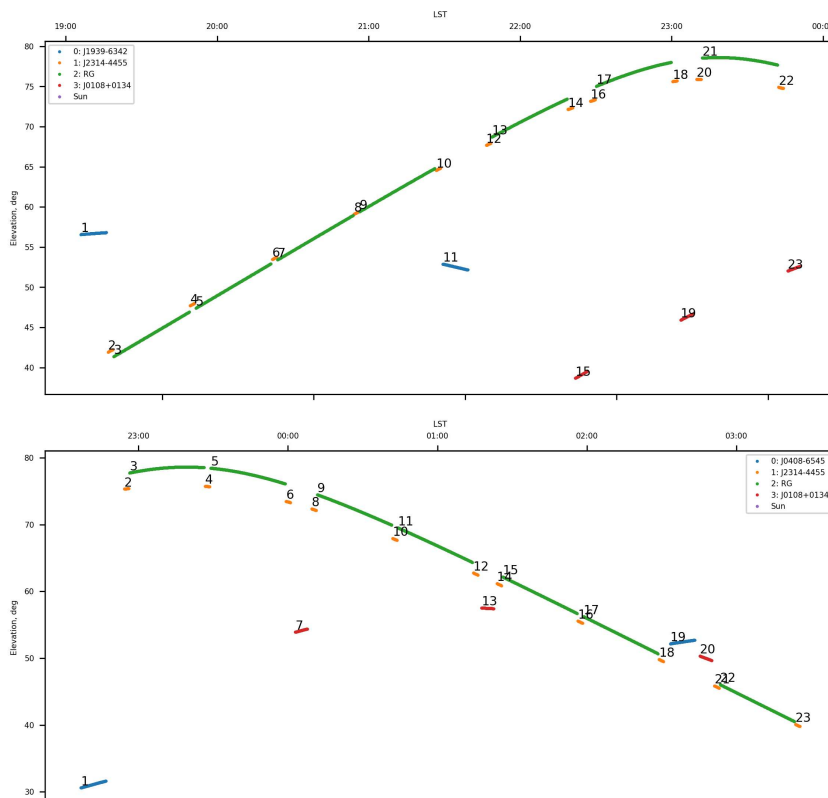


**Figure 15.** *Top:* elevation plot of the first observation. *Bottom:* elevation plot of the second observation.

The correlator was configured to record full polarization products with an integration time of 8 seconds.

The two observations were planned in order to maximize the u-v plane coverage. The elevation plots of the source and calibrators for each observation is presented in Figure 15.

Despite some contamination from RFI near the band edges, the central portion of the band was largely clean. The data quality was considered suitable for polarization and spectral analysis, with successful calibration achieved in both observing runs.

The observed calibrators are:

- **Bandpass and flux calibrator:** J1939–6342 (first observation), J0408–6545 (second observation)
- **Gain calibrator (amplitude and phase):** J2314–4455
- **Polarization angle calibrator:** J0108+0134

## 6.2 Data reduction and imaging

The data reduction workflow has been implemented using several software tools. The primary reduction steps -flagging, calibration, and self-calibration- were performed using the CARACAL pipeline (Józsa et al., 2022). Additional steps employed CASA (for data splitting and image convolution), SoFiA (Offringa, 2010; Serra et al., 2015) for masking, and WSclean (Van der Tol et al., 2018) for imaging in both total intensity and polarization.

### 6.2.1 From calibration to imaging

Each of the two MeerKAT observations was initially reduced independently, according to the following procedure:

1. **Calibrator extraction:** The calibrators were extracted into a separate Measurement Set using CARACAL. The spectral channels were binned in groups of five, corresponding to  $\sim 1$  MHz per bin.
2. **Flagging:** Flagging of radio-frequency interference was performed in three stages: two iterations using AOFlagger and one using Tricolour (Hugo et al., 2022), to minimize RFIs across the band.
3. **Calibration:** Calibration tables were generated for phase, amplitude, bandpass, and cross-hand polarization (X-Y phase and leakage) solutions.
4. **Target extraction and calibration:** The target field was extracted into a separate MS and Calibration solutions were applied on the fly during the extraction.
5. **Target flagging:** A two-step flagging strategy was applied to the target data to remove residual RFI and bad visibilities.
6. **Binning:** As a final step, the target was binned every 5 channels.

The two calibrated and binned target datasets were then combined into a single Measurement Set. Self-calibration was then performed.

Polarization calibration was performed using the `polcal` task from the CARACAL pipeline, which handles the calibration of instrumental leakage and polarization angle, following Loi et al. (2025). The polarization calibrator used was J0108+0134. This source is widely adopted in MeerKAT L-band observations due to its high brightness and favorable sky position at southern latitudes. Its polarization properties -fractional polarization and polarization angle- have been well characterized and validated for MeerKAT calibration (Taylor and Legodi, 2024).

Polarization calibration includes the following steps:

- **Cross-hand delay calibration (KCROSS):** Solves for the relative delay between the orthogonal feed polarizations (X and Y). This step ensures that the frequency-dependent phase slope between the two polarization channels is removed, allowing the cross-hand visibilities to be coherently combined.
- **XY-phase calibration (Xf):** Corrects the constant phase offset between the polarization channels after the cross-hand delay is removed. This aligns the polarization basis such that the Stokes parameters are formed correctly and the orientation of the Q–U plane is physically meaningful.
- **Leakage calibration (Df):** Determines the instrumental polarization leakage (D-terms), i.e. the mixing of Stokes I into Q and U due to imperfections in the feeds. This is done by observing a source over a range of parallactic angles, enabling the separation of true sky polarization from instrumental effects.

The resulting calibration tables—D-terms, XY-phase delay, and polarization angle—were applied to the target data, allowing for reliable imaging of the polarized emission in Stokes Q and U. Stokes V was not imaged in this work because synchrotron radiation, from the sources studied in this work, produces negligible amounts of circular polarization.

Imaging of the calibrated polarization data was performed using WSClean. Only the frequency range from 900 to 1400 MHz was used, as the frequencies between 1.4 and 1.6 GHz suffer from strong off-axis leakage.

## 6.2.2 Imaging

The final total intensity image (visible in Section 7.1) was produced using WSClean with Briggs weighting and a robust parameter of 0, leading to a synthesized beam of 7.6" by 7.3". In order to avoid cleaning strong artifacts, which can be identified as sources, the cleaning procedure was performed using a mask. In particular, a preliminary cleaned image was used to produce two masks using SoFiA, one focused on compact sources and one on extended emissions, later combined into a single one.

In preparation for the data analysis reported in Section 7, spectral cubes with different purposes were produced.

For the spectral analysis (Section 7.2), the calibrated visibilities were divided into 10 equal frequency sub-bands. Each sub-band was imaged separately using the same WSClean parameters used before, followed by two correction steps:

- All images were convolved to a common resolution of  $10 \text{ arcsec} \times 10 \text{ arcsec}$  using the CASA task `imsmooth`.
- Each image was divided by the corresponding primary beam response in its frequency range, to correct for the frequency-dependent sensitivity of the telescope. This correction followed the method described in Mauch et al. (2020).

An example of the primary beam correction map, computed for the Multi-Frequency Synthesis (MFS) image centered at 1.25 GHz, is shown in Figure 16.

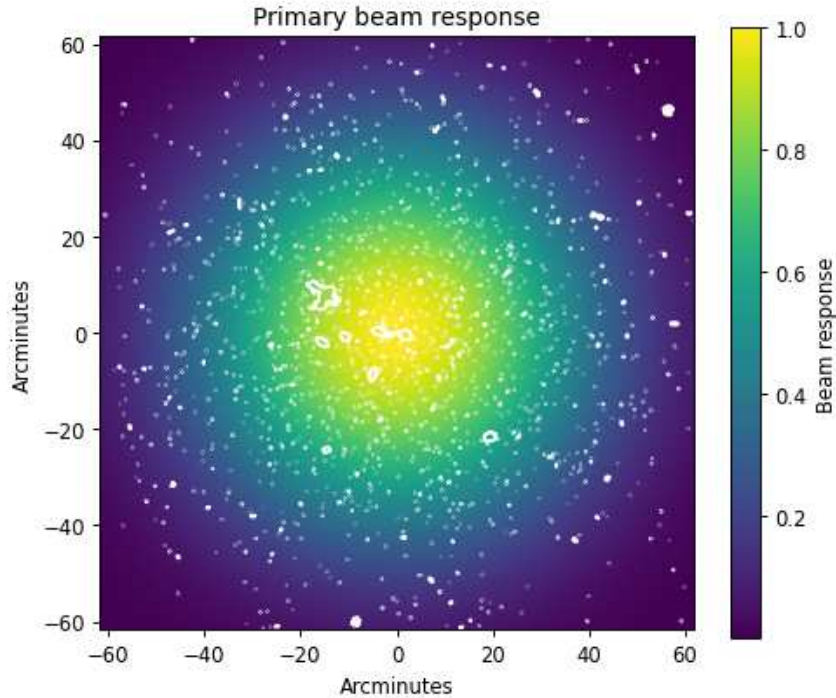


**Figure 16.** Primary beam correction map for the MeerKAT MFS image at 1.25 GHz. The correction accounts for the frequency-dependent off-axis gain response drop-off. The white lines represent the  $8\sigma$  contours with  $\sigma = 10^{-5}$  of the image to show the position of the extended sources.

Dividing the MeerKAT bandwidth into sub-bands requires particular attention, as RFIs are not uniformly distributed across the frequency range. To identify the most affected regions, we examined the cumulative amplitude of the visibilities as a function of frequency, as shown in Figure 17.

In an ideal scenario, the amplitude distribution would follow a smooth power law, reflecting the combined spectral indices of all sources within the primary beam. However, gaps appear in the distribution due to a higher fraction of flagged visibilities at specific frequencies, corresponding to strong RFI contamination. This pattern is consistent with the RFI distribution observed by Sihlangu et al. (2022), where they tends to occupy well-defined frequency chunks across the L-band.

This non-uniform flagging introduces differences in the UV coverage across sub-bands, which affects the flux response at different spatial scales. In particular, short baselines are more susceptible to RFI flagging, resulting in the loss of sensitivity to large-scale emission, the component we are more interested in this work.

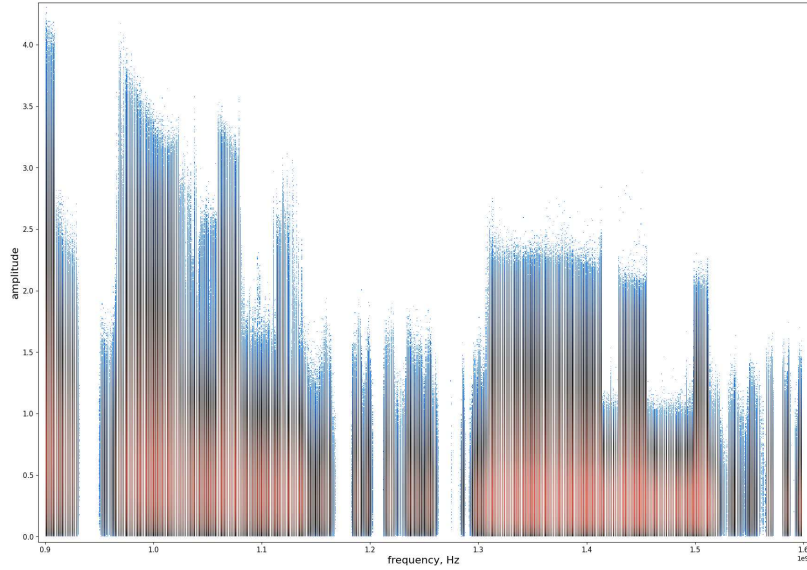
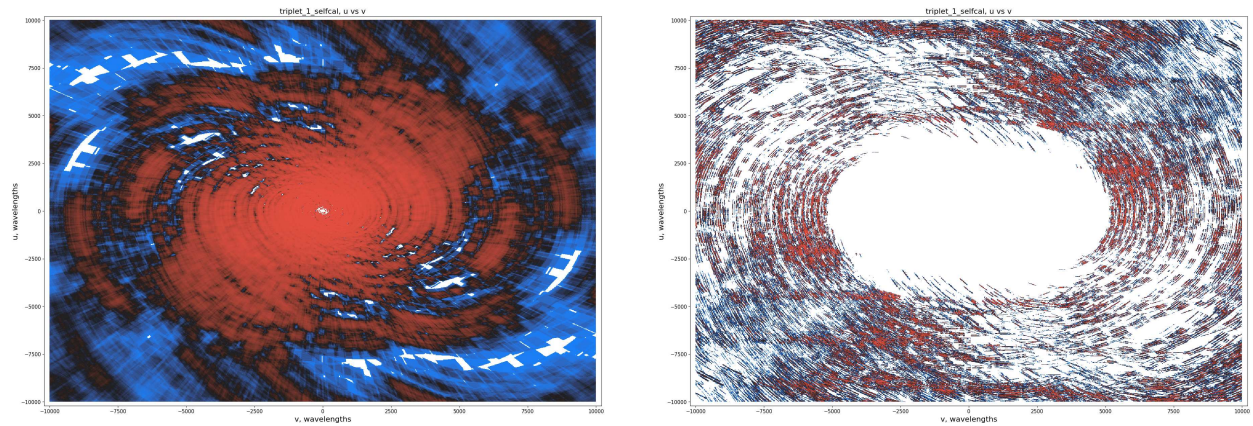


**Figure 17.** Cumulative amplitude of the visibilities (XX correlation) as a function of frequency. The color scale reflects the density of data points. Frequencies with no visibilities correspond to spectral channels that were completely flagged due to RFI contamination.

Figure 18 illustrates the difference in UV coverage between two representative sub-bands: the second (covering 0.97–1.04 GHz) and the last (1.53–1.60 GHz). It is evident that the visibilities in the shorter baselines are significantly less dense in the higher-frequency sub-band, highlighting the impact of RFI on spatial scale sensitivity.



**(a)** UV coverage for sub-band 2 (0.97–1.04 GHz).

**(b)** UV coverage for sub-band 10 (1.53–1.60 GHz).

**Figure 18.** Comparison of UV coverage between two sub-bands. The higher-frequency sub-band shows a significant loss of short baselines, leading to reduced sensitivity to extended emission.

Multi-frequency synthesis images of Stokes Q and U have been produced by averaging across the usable frequency band. These images provide a first look at the polarized emission, but are still affected by bandwidth depolarization from Faraday rotation effects. This issue is treated using rotation measure synthesis (see Section 7.3), which allows the recovery of the intrinsic polarization properties and Faraday depth structure.

The RM Synthesis analysis requires the production of spectral cubes for stokes Q and U. Considering the need of a compromise between frequency resolution and signal-to-noise ratio, the data was binned in 4 MHz intervals, resulting in 125 frequency channels across the 900–1400 MHz band. Each channel was independently imaged in Stokes I, Q and U using WSClean and then combined using internal functions. The resulting image cubes were then convolved to a common angular resolution.

## Data Analysis

This section presents the analysis performed using the MeerKAT data. In particular, Section 7.1 presents an analysis on the morphology of the source, Section 7.2 analyses the spectral properties both in-band and using other measurements and Section 7.3 investigate the source from a polarimetric point of view.

### 7.1 Morphology

The study of the radio morphology of active galactic nuclei provides crucial insight into their classification, physical processes, and interaction with the surrounding medium. In particular, the large-scale structure of the jets and lobes constrains the dynamical evolution of the radio source, while the core properties reflect the accretion and jet-launching mechanisms. Previous studies of this object, primarily based on X-ray and  $\gamma$ -ray observations, have classified it as a BL Lacertae-type blazar (see Section 2.3). However, such high-energy observations do not reveal the extended radio structure that is essential for assessing its large-scale morphology and environmental impact.

Figure 19 shows the total intensity image from the analysis of MeerKAT presented in this thesis.

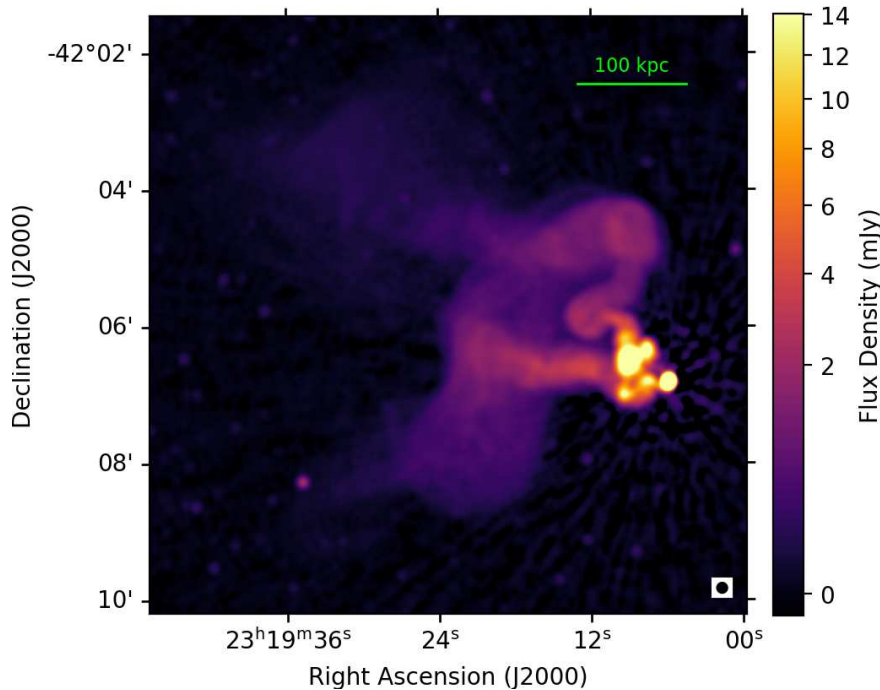


**Figure 19.** MFS image obtained from MeerKAT data centred at 1.25 GHz, with a synthesized beam of  $7.6'' \times 7.2''$ , a pixel scale of 1.5 arcsec/pixel and a RMS of  $6 \mu\text{Jy}/\text{beam}$ .

As expected for a standard radio-loud AGN, we can easily identify the core and the extended radio emission of the target.

The core appears as the bright, unresolved radio source on the west side of the image, from

which two outflows clearly emerge. Further from the core, two distinct plumes become evident, both unusually bent towards the east of the image, and they also seem to terminate in what may be compression shocks or adiabatic expansions.

The northern plume appears more twisted and fades at its end, whereas the southern one is less turbulent, slightly broader, and appears more extended. The maximum projected separation between the core and the northern emission is approximately 415 kpc, while the southern emission extends over 300 kpc, though it appears broader.

These projected measurements, however, are not representative of the true dimension of the radio galaxy, which could be larger along the line of sight. At this stage, it is not possible to determine which plume is oriented toward us and which is receding, but the polarization data is useful for this purpose (see Section 7.3). The limited spatial resolution, together with the complexity and overlapping of structures, prevents a direct tracing of the jets back to the core.

These extended and twisted lobes are extremely peculiar. In fact, the emission from the core is spatially coincident with the known blazar position, and aligns with the brightest cluster galaxy (BCG) of Abell S1111, as seen in optical images from the DESI Legacy Survey (Figure 7). However, in an ideal scenario, a Blazar, or more generally an FR I-type radio galaxy viewed at a small inclination angle, would be expected to exhibit two symmetric jets relatively close to the core, with the jet oriented toward the observer appearing brighter due to Doppler beaming.

Also, blazars typically do not display such extended radio emission, as already said in Section 2.3.

Another notable feature of this source is the presence of filamentary structures, which may either lie within each plume or potentially connect the two, as seen in similar cases such as Ramatsoku, M. et al. (2020). These scenarios may imply the presence of large-scale magnetic fields either within the lobes themselves or extending beyond the main body of the radio emission.

To better visualize the filamentary structures and emphasize local brightness variations, a Sobel filter (or gradient magnitude filter) was applied to the image, as shown in Figure 20. This technique, commonly used in X-ray imaging to highlight filaments or shocks in the intracluster medium, has also been used in other contexts to enhance edge-like features.

In this case, the region near the core becomes saturated due to the inability to disentangle the jet from the bright central emission, however, the inner structure of the plumes is more clearly revealed.

A Sobel filter leaves 'holes' where the light intensity stays relatively constant, allowing us to better see the direction of the jets. Here is even more evident how the southern jet appears much more collimated than the northern one.

It is possible to note a remarkably long filament, extending  $\sim 180$  kpc, which appears to originate from the eastern part of the southern lobe bending towards the west curve portion of the northern lobe. The northern edge also becomes more visible in the filtered image.

Taking into account these considerations, it is possible to visually analyse some of the morphological classifications previously attributed to this object, discussed in Section 4. Despite the peculiar orientation of the source, viewed close to the jet axis, several characteristic features of FR I morphology are still apparent: the gradual decrease in surface brightness with distance from the core, the presence of compact hotspots near the central region, the fading and diffusion of the jets as they extend outward from the core.

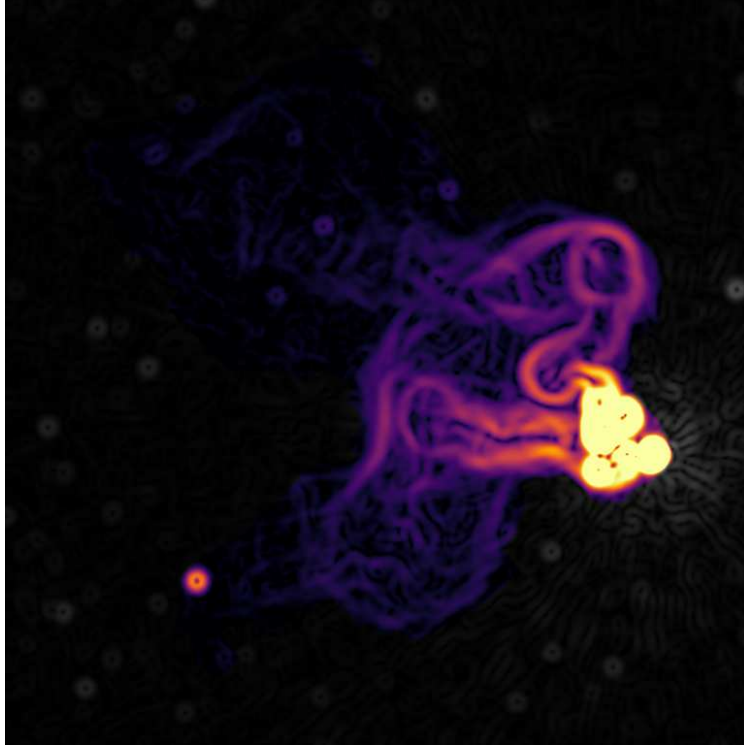


**Figure 20.** The image shows the application of a Sobel Filter to the target.

Furthermore, the host galaxy is a giant elliptical located at the centre of a galaxy cluster, another characteristics of FR I sources. Both of these features support the FR I classification even in this blazar-like orientation, which would be consistent with the AGN unification scheme.

The overall morphology seems to resemble that of the radio galaxy 3C31, shown in the top image in Figure 4 (Laing et al., 2008), which exhibits similar jet structures and diffuse plumes, but viewed from a different angle.

## 7.2 Spectral Analysis

This section aims to show the spectral analysis from the total intensity results. Section 7.2.1 reports an in-band spectral fitting performed with MeerKAT data, and the solution proposed to the problems encountered. Section 7.2.2 includes measurement from other instruments and from the literature. A discussion on the spectral ageing is reported in Section 7.2.3.

### 7.2.1 In-band MeerKAT Spectral Index

Following the data reduction process described in Section 6.2, we produced ten images for this spectral analysis, one for each spectral sub-band.

As discussed in Section 6.2, the flux density response across sub-bands is non-uniform, primarily due to the uneven distribution of flagged visibilities. An additional source of variation arises from the deconvolution process: in noisier images, the cleaning algorithm reaches its stopping criterion earlier, leading to an underestimation of the total flux.

To mitigate these issues, we adopted a correction method to improve the flux density estimation based on the images themselves. In particular, a first-order correction was applied

to recover the flux in compact components such as the core and hotspots.

The correction method exploits bright unresolved sources in the field, under the assumption that their spectra follow a power-law distribution in the 0.9–1.6 GHz range. A Python script was developed to identify the brightest unresolved sources surrounding the target.

Each source was modelled with a Gaussian fit and sorted by flux density. For each source, a power-law fit of the fluxes was performed, and the resulting correction factors were derived for each sub-band.

The average correction from the eight brightest sources, of the order of 1-3%, was then used to normalize the response across all sub-bands.

Despite these corrections, the in-band spectra still exhibit scatter and flux density loss in sub-bands affected by strong RFI and poor UV coverage, as previously discussed. By visually inspecting the UV coverage and image quality, sub-bands 1, 2, 3, 7, and 8 were identified as the most representative of the true flux density response. These sub-bands were therefore used for the spectral measurements of the extended emission.

With these corrections in place, the resulting integrated flux densities follow a power-law distribution, as shown in Figure 21.

The integrated flux density of the radio galaxy was then calculated using the  $3\sigma$  mask obtained from the MFS image and then scaled using the derived correction coefficients. The flux density uncertainty in each sub-band was estimated by adding in quadrature the standard deviation of the normalization factors and the local RMS noise in the image, the latter contributing two order of magnitude less than the former.

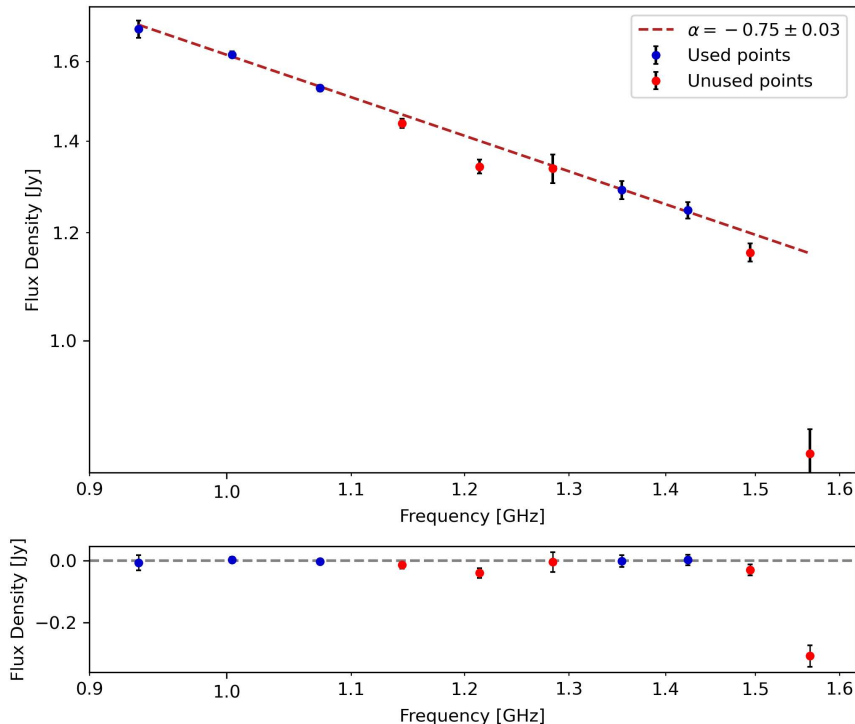


**Figure 21.** *Top:* integrated flux densities measured in each sub-band. The power-law fit (dashed line) was performed using only sub-bands 1, 2, 3, 7, and 8, which were considered more reliable due to better UV coverage and lower contamination from RFI. *Bottom:* residuals from the power-law fit.

The resulting spectral index is  $\alpha = -0.75 \pm 0.03$ , consistent with the typical values in radio galaxies.

To investigate the spatial variation of the spectral index across the source, we constructed an in-band spectral index map using the same sub-band images adopted for the spectral analysis. All images were first convolved to a common resolution of 10 arcseconds and corrected using the response normalization values derived from the unresolved field sources. The flux densities of each pixel, across the images of sub-bands 1, 2, 3, 7, and 8, were then fitted using a power law.

The uncertainty in each pixel’s intensity was estimated by multiplying the flux density value by the standard deviation of the normalization factors as before. The spectral index uncertainty was then computed using standard error propagation applied to a weighted least-squares fit, accounting for both the flux density scale and the logarithmic transformation. The resulting spectral index map and associated errors is shown in Figure 22.

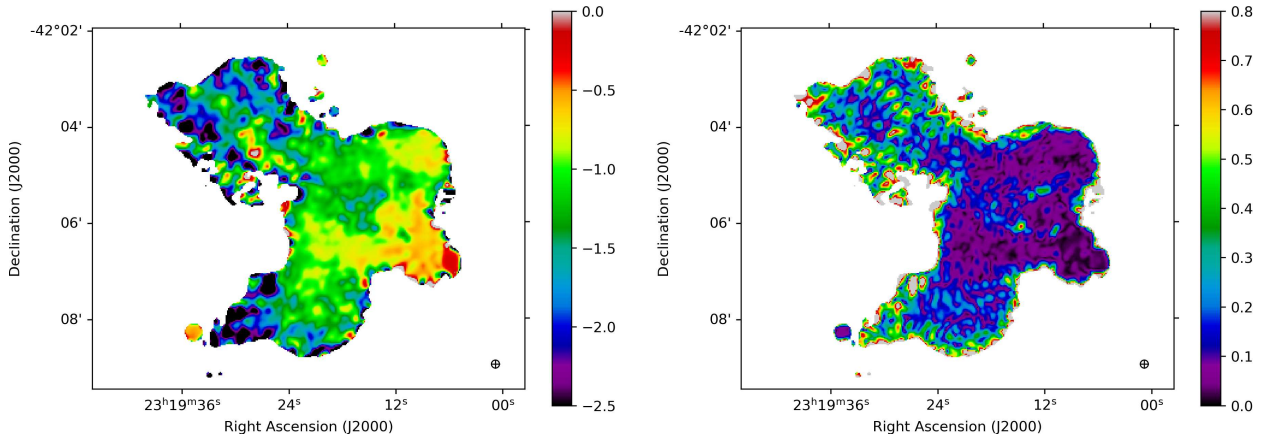


**Figure 22.** *Left:* MeerKAT in-band spectral index map of the target radio galaxy, computed from sub-bands 1, 2, 3, 7, and 8. The colour scale represents the spectral index  $\alpha$ . *Right:* associated errors.

The flattest value of spectral index is found at the bright compact region in the lower right, corresponding to the radio core. From there, the spectral index steepens progressively along the jets, following the same trend as the surface brightness. This is a typical behaviour in radio galaxies, indicating spectral ageing of the relativistic electrons as they propagate away from the core.

To further improve the analysis of the spectral structure of the source, we performed spectral fitting in key regions of the radio galaxy, using aperture photometry to estimate the enclosed flux density. This method was applied to extended components such as the plumes, a regular part of the inner jet, and a bright hotspot. For the core, treated as an unresolved source, the flux density was measured by fitting a two-dimensional Gaussian model with amplitude, standard deviation, and centroid position as free parameters, automatically obtained using a  $\chi^2$  minimization.

The resulting flux densities from these apertures were used to derive localized spectral indices, shown in Figure 23.

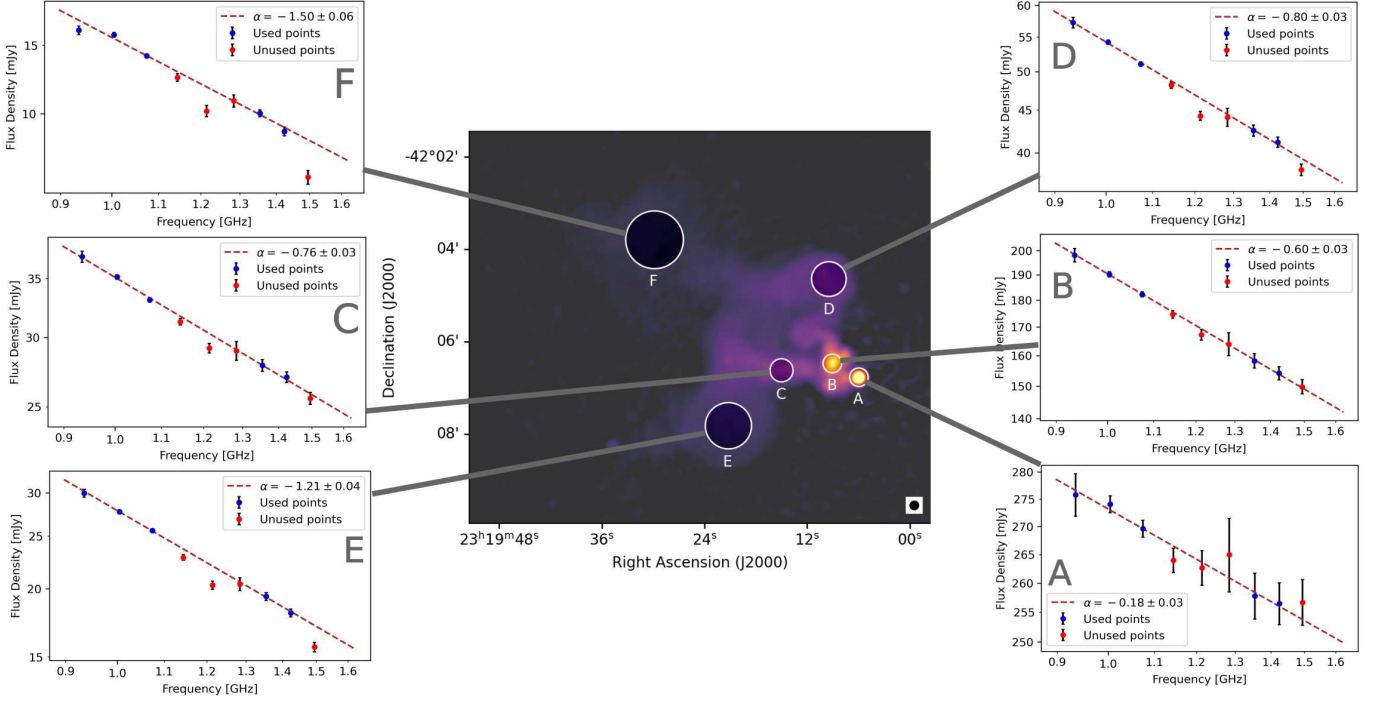


**Figure 23.** The image shows the in-band spectral fitting in different positions of the target.

The spectral index starts from values of  $\alpha \approx -0.2$  in the core and steepens to  $\alpha < -1.5$  in the outermost parts of the emission. Again, this is consistent with the scenario of electrons being injected by the core and the gradual ageing due to energy losses as they travel far from it.

### 7.2.2 Integrated Spectral Index

To perform a more comprehensive spectral analysis, all previously available integrated flux density measurements from the NASA/IPAC Extragalactic Database (NED) were considered. In addition, recent measurements were extracted directly from public images obtained through the GLEAM (The GaLactic and Extragalactic All-sky MWA survey, Wayth et al. (2015)) and RACS (Rapid ASKAP Continuum Survey, McConnell et al. (2020)) surveys, using a  $3\sigma$  contour to estimate the integrated flux density.

The following flux densities were obtained from direct measurements on radio images:

Instrument	Survey	Central Frequency [MHz]	Flux Density [Jy]
MWA	GLEAM	88	$7.02 \pm 0.36$
MWA	GLEAM	118	$5.45 \pm 0.29$
MWA	GLEAM	155	$4.63 \pm 0.24$
MWA	GLEAM	200	$3.92 \pm 0.20$
ASKAP	RACS	888	$1.65 \pm 0.08$
MeerKAT		1250	$1.35 \pm 0.07$
ASKAP	RACS	1368	$0.99 \pm 0.05$
ASKAP	RACS	1656	$0.78 \pm 0.04$

The following measurements were taken from pre-existing radio source catalogues, in particular, using the Culgoora radio telescope (Slee, 1995), the Parkes Radio Sources Catalogue (Wright and Otrupcek, 1990), the Molonglo Observatory synthesis telescope (Mills, 1981) and the Australian Telescope 20 GHz Survey (Murphy et al., 2010).

Telescope	Catalogue	Frequency [MHz]	Flux Density [Jy]
Culgoora		80	$6.00 \pm 0.60$
Culgoora		160	$3.00 \pm 0.30$
Parkes	PKSCAT90	408	$1.67 \pm 0.17$
Parkes	PKSCAT90	635	$2.02 \pm 0.20$
MOST		843	$1.61 \pm 0.16$
Parkes	PKSCAT90	1410	$1.00 \pm 0.10$
Parkes	PKSCAT90	2700	$0.74 \pm 0.07$
Parkes	PKSCAT90	5000	$0.54 \pm 0.05$
Parkes	PKSCAT90	8400	$0.27 \pm 0.03$
ATCA	AT20G	20000	$0.15 \pm 0.02$

For the image-based measurements, flux density uncertainties were calculated using the following formula:

$$\sigma S_\nu = \sqrt{(f \cdot S_\nu)^2 + N_{\text{beam}} \cdot \text{RMS}^2} \quad (37)$$

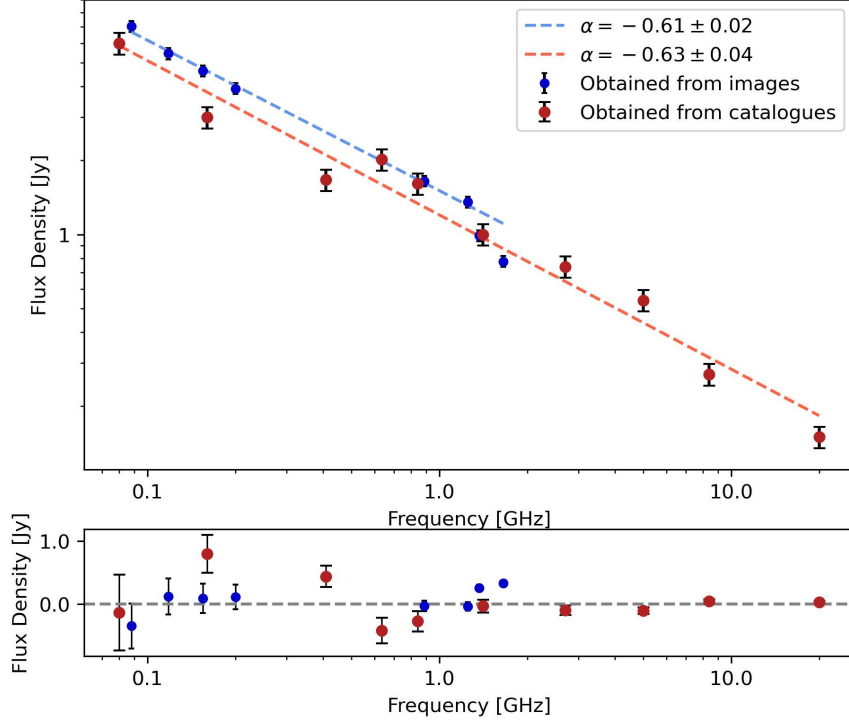
where  $f = 0.05$  is a fractional uncertainty representing calibration or systematic errors, and  $N_{\text{beam}}$  is the number of synthesized beams within the source area. The RMS is the root mean square noise in the surrounding background cold sky. For catalogue-based measurements, the tabulated uncertainties, when available, were used. Otherwise, an uncertainty of 10% of the flux density value was adopted.

Figure 24 shows the resulting flux densities vs frequency plotted in log–log space, to evaluate the integrated spectral energy distribution.

It is evident that the ASKAP 1368 and 1656 MHz measurements underestimate the flux density, likely due to poor image quality and cleaning artifacts introduced by the bright blazar core, as said in Section 4. The catalogue-based flux densities, on the other hand, show a higher scatter around the fit, possibly due to differences in measurement methods or intrinsic variability of the source itself.

Power-law fits were performed in log–log space for both datasets, excluding the ASKAP 1368 and 1656 MHz measurements from the image-based fit. The resulting spectral indices are:

$$\begin{aligned} \alpha_{\text{images}} &= -0.61 \pm 0.02 \\ \alpha_{\text{catalogs}} &= -0.63 \pm 0.04 \end{aligned}$$



**Figure 24.** *Top:* integrated radio spectrum of the source. Flux measurements from the literature (catalogs) and from image-based extraction are shown. A power-law fit was performed separately for each set. *Bottom:* residuals from the fit.

We can also restrict the analysis to include only the most recent and highest-quality measurements, specifically GLEAM, RACS low, MeerKAT, and ATCA, all taken from images, with the sole exception of the latter. The trend suggest a spectral break, allowing for a double power-law fit, with the following values:

$$\begin{aligned} \alpha_{\text{low}} &= -0.61 \pm 0.02 && (88\text{--}1250 \text{ MHz}) \\ \alpha_{\text{high}} &= -0.79 \pm 0.04 && (1.25\text{--}20 \text{ GHz}) \end{aligned}$$

Considering the difference between the spectral index value in the lower frequencies and the in-band of MeerKAT we can assume that change of slope occurs at  $\sim 1$  GHz.

This spectral steepening at higher frequencies is consistent with synchrotron ageing, where energy losses cause a curvature in the radio spectrum.

### 7.2.3 Spectral Ageing

Building on the results of the previous sections, we now investigate the spectral ageing of the electron population by fitting a simple Continuous Injection (CI) model to the integrated spectrum.

The CI model assumes that a population of relativistic electrons is continuously injected into a region with a uniform magnetic field, an isotropic pitch angle distribution, and negligible expansion. The resulting synchrotron spectrum is described by a power law with  $S_\nu \propto \nu^{\alpha_{\text{inj}}}$  below a characteristic break frequency  $\nu_b$ , and steepens to  $S_\nu \propto \nu^{\alpha_{\text{inj}}-0.5}$  above it.

This model is typically applicable to regions such as cores or compact hotspots, and may be less suitable for large-scale, spatially diffuse structures such as radio lobes. Nevertheless, it provides useful information on spectral curvature of the integrated emission.

To estimate the injected spectral index, the break frequency and relative normalization, a  $\chi^2$  minimization was performed using synthetic spectra generated with the **Synage++** package (Murgia et al., 1999). The resulting best-fit parameters are:

$$\alpha_{\text{inj}} \approx -0.52$$

$$\nu_b \approx 9.23 \text{ GHz}$$

The CI model fit is shown in Figure 25.

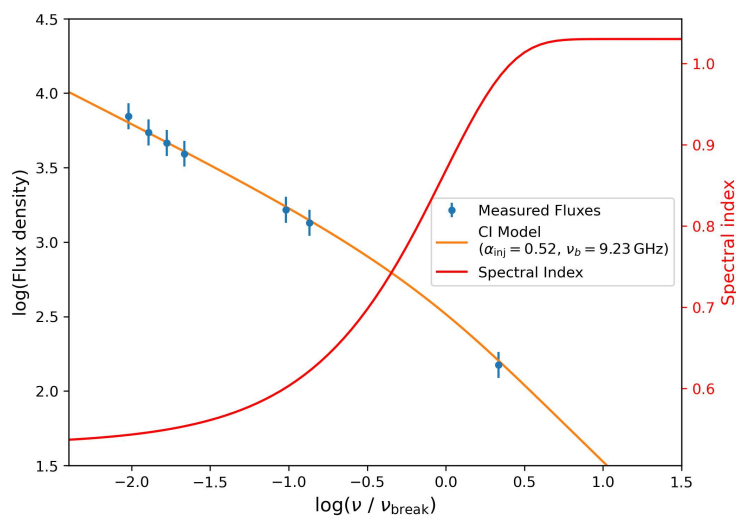


**Figure 25.** Fit to the integrated flux measurements using a CI model. The plot includes the input data points with a 5% error and the derived spectral index on the right.

Although the model provides a good fit to the observed data, physical validation requires comparison with a more suitable model for extended emission. The Jaffe–Perola (JP) (Jaffe and Perola, 1973) model offers such an alternative.

Unlike the CI model, the JP model describes a scenario in which a population of electrons is injected in a single burst and subsequently evolves via synchrotron and inverse Compton losses, with continuous isotropization of the pitch angles. This model is particularly appropriate for describing the oldest parts of the lobes, such as the outermost regions of the jets.

While the bandwidth of the MeerKAT data is insufficient to directly observe a clear steepening within the in-band spectra, it is still possible to estimate the local break frequency under the assumption of a fixed injection index. For a given  $\alpha_{\text{inj}}$ , we can use the spectral index at a specific frequency to derive a unique break frequency, according to the JP model.

Following this approach, we used the in-band spectral index map (from Figure 22) to compute the break frequency at each pixel, assuming the same  $\alpha_{\text{inj}} = -0.52$  as derived from the CI fit. The resulting break frequency map is shown in Figure 26.

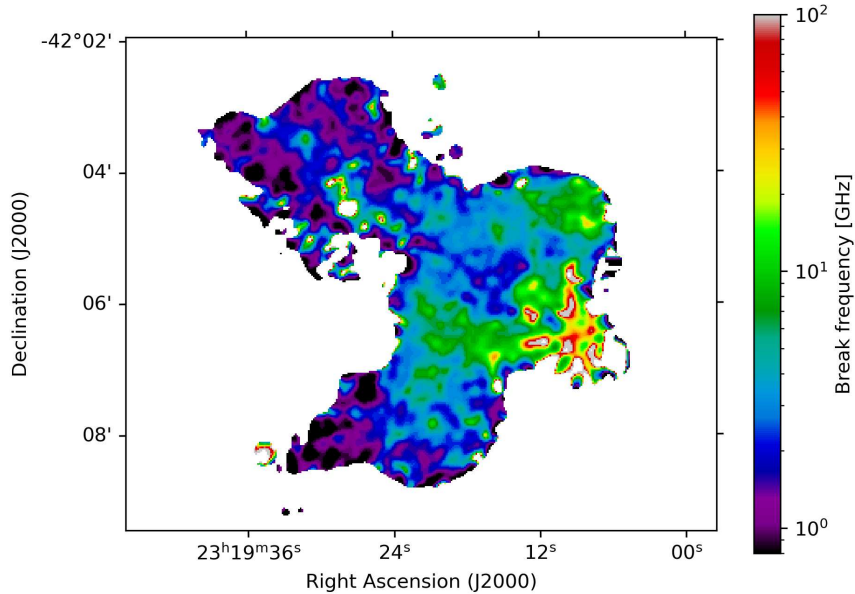


**Figure 26.** Map of break frequencies derived from the in-band spectral index, assuming a fixed injection index  $\alpha_{\text{inj}} = -0.52$  and using the Jaffe–Perola model. Lower break frequencies correspond to older electron populations.

The lowest break frequencies, found in the northern lobe, are below 1 GHz. These correspond to the oldest regions of the source, and are inconsistent with the one obtained from the CI model. The discrepancy between the break frequencies derived from the two models is expected. The CI model assumes continuous injection into a homogeneous region and does not account for the complex morphology, environmental interactions, or multiple episodes of activity, all of which are likely relevant in this source, especially given the strong central core, bent jets, and diffuse plumes. This makes the CI model too simple to describe this source.

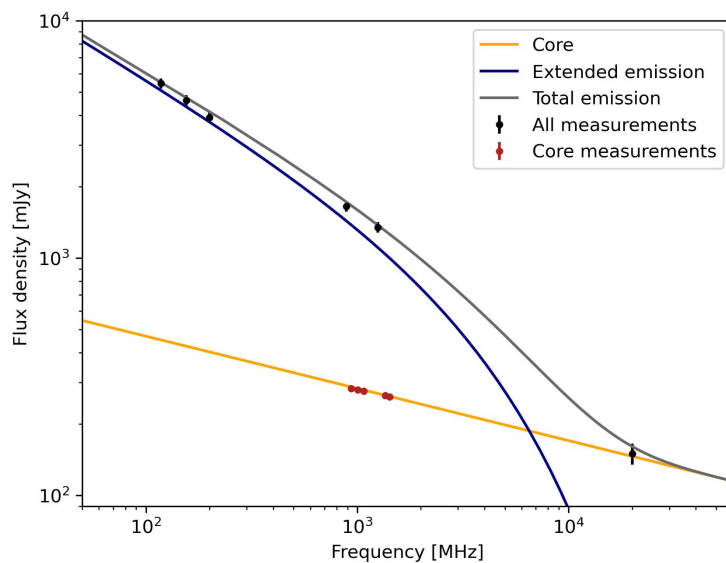


**Figure 27.** The figure shows the fit for the core and extended emission separately, showing that the integrated flux is better described by summing the two components.

A more realistic approach involves adopting a  $CI_{\text{off}}$  model, as described in Murgia, M. et al. (2011), which incorporates a finite injection time and a subsequent quiescent phase. Such a model would be better representative for a source in a remnant or dying phase.

Finally, an interesting observational constraint is provided by the 20 GHz flux measurement. This point appears consistent with the extrapolation of the core's spectral index as determined from the MeerKAT in-band spectrum, suggesting that the high-frequency emission is dominated by the compact core. If we separately fit the core flux with a power law and the extended emission with a JP model with a lower break frequency than before, the integrated flux is described better, as shown in Figure 27.

It is clear that measurements between 1.25 GHz and 20 GHz are crucial to better characterize the spectral behavior of the source and to disentangle the contributions from the core and the extended jets and lobes.

According to synchrotron theory (Blumenthal and Gould, 1970), the break frequency  $\nu_b$  can be related to the time elapsed since the last particle acceleration episode using the following expression:

$$t_{\text{syn}} = 1590 \frac{B^{1/2}}{(B^2 + B_{\text{IC}}^2)[(1+z)\nu_b]^{1/2}} \quad [\text{Myr}] \quad (38)$$

Here,  $B$  is the magnetic field in  $\mu\text{G}$ ,  $\nu_b$  is the break frequency in GHz, and  $B_{\text{IC}}$  is the equivalent inverse Compton magnetic field from the cosmic microwave background (CMB), given by:

$$B_{\text{IC}} = 3.25(1+z)^2 \quad [\mu\text{G}] \quad (39)$$

To estimate the magnetic field strength, we adopt the equipartition condition, following the formalism described in Govoni and Feretti (2004). The equipartition magnetic field  $B_{\text{eq}}$  is given by:

$$B_{\text{eq}} = \left( \frac{24\pi}{7} u_{\text{min}} \right)^{1/2} \quad (40)$$

where the minimum energy density  $u_{\text{min}}$  is computed as:

$$u_{\text{min}} = \xi(\alpha, \nu_1, \nu_2) (1+k)^{4/7} (\nu_0 [\text{MHz}])^{-4\alpha/7} (1+z)^{(12-4\alpha)/7} \left( I_0 \left[ \frac{\text{mJy}}{\text{arcsec}^2} \right] \right)^{4/7} (d [\text{kpc}])^{-4/7} \quad (41)$$

In this expression,  $\xi(\alpha, \nu_1, \nu_2)$  is a constant that depends on the spectral index  $\alpha$  and the frequency integration limits  $\nu_1, \nu_2$ ;  $k$  is the proton-to-electron energy ratio (typically assumed to be 1);  $I_0$  is the surface brightness at the reference frequency  $\nu_0$ ;  $d$  is, in this case, the thickness of the jets and  $z$  is the redshift.

Assuming the thickness of the jets to be  $\sim 150$  kpc, the spectral index and surface brightness found before, we obtain an equipartition magnetic field strength of  $B \approx 1.35 \mu\text{G}$ . For  $z = 0.055$ ,  $B_{\text{IC}} \approx 3.6 \mu\text{G}$ .

Using the break frequency map derived from the JP model (see Section 7.2.2), we compute the synchrotron age at each pixel. The resulting radiative age map is shown in Figure 28.

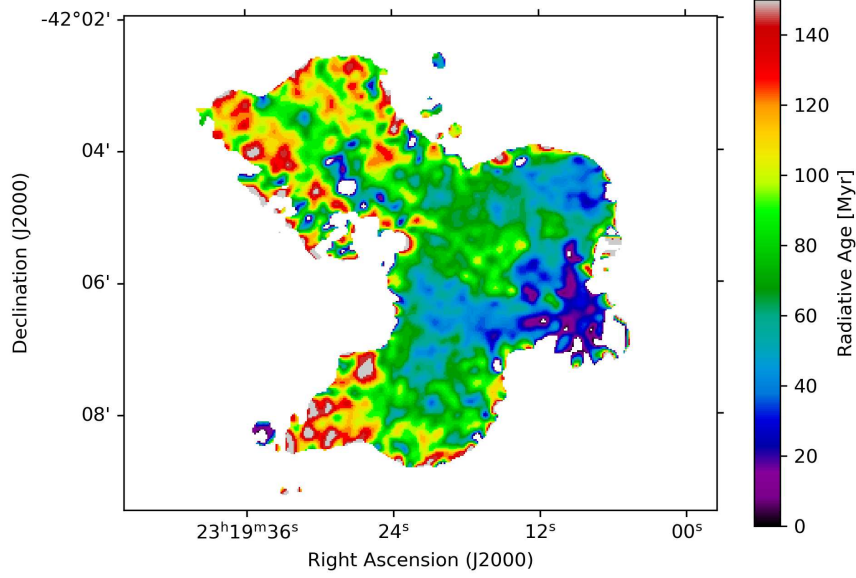


**Figure 28.** Radiative age map derived from the break frequency map using the JP model and an equipartition magnetic field of  $B = 1.35 \mu\text{G}$ .

In the northern lobe, where the lowest break frequencies are observed, the plasma has a synchrotron age of more than 100 Myr.

It is important to note that small uncertainties in the magnetic field strength do not strongly affect the age estimates when  $B \sim B_{\text{IC}}$ , as shown in Parma et al. (1999). In this regime, radiative losses are dominated by inverse Compton scattering, and the age becomes relatively insensitive to small variations in  $B$ . This is visible in Figure 29.

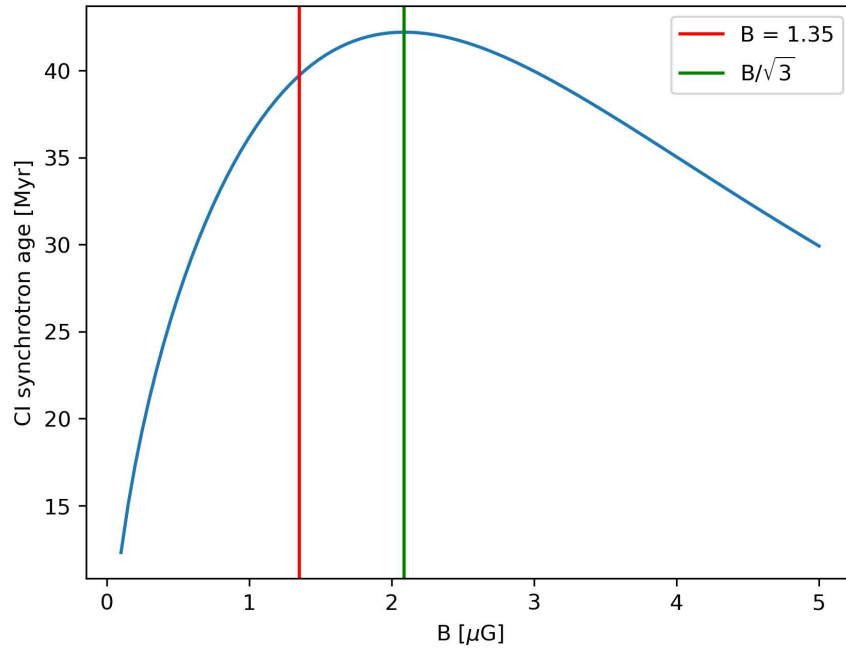


**Figure 29.** The figure shows the effects of the value of magnetic field on the estimate of synchrotron age, computed using the break frequency found using the CI model.

### 7.3 Polarization analysis

The steps reported in Section 6.2 produced the I, Q, and U Stokes images with the signal averaged across the band 0.9 GHz to 1.4 GHz. This is an approximation and is used for a quick look analysis rather than a complete one, carried out in the next section.

The polarized images are presented in Figure 30 and it is clear that the source presents non-negligible Stokes U and Q components.

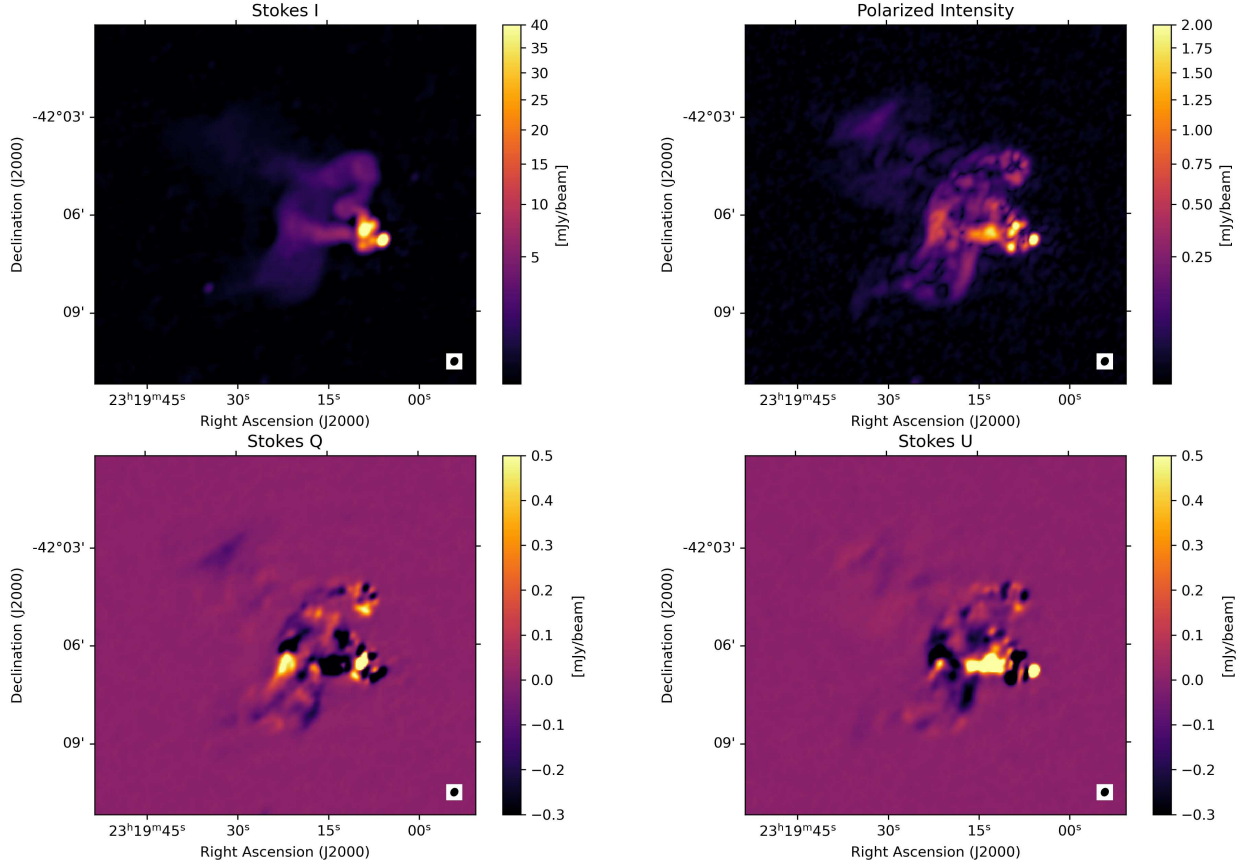


**Figure 30.** *Top:* the images show the Stokes I and polarized images, obtained by averaging the signal across 0.9-1.4 GHz with a beam size of 12.5"x10". *Bottom:* images showing Stokes Q and U components obtained as before.

The polarized intensity has been obtained by summing in quadrature Stokes Q and U images, but this produces a bias caused by summing in quadrature the noise, which usually oscillates around zero. To correct for this, a local map for the background was computed for the two Stokes components, then the two standard deviations of the signals were found, they were summed in quadrature, obtaining a value of  $\sigma_{QU} = 4 \mu\text{Jy}/\text{beam}$  which was subtracted from the polarized intensity image.

The polarized components are better visualized by computing the fractional polarization and the polarization angle, in the following way:

$$f_{\text{pol}} = \frac{\sqrt{Q^2 + U^2} - \text{bias}}{I} \quad \chi = \frac{1}{2} \arctan\left(\frac{U}{Q}\right) \quad (42)$$

and are presented in Figure 31.

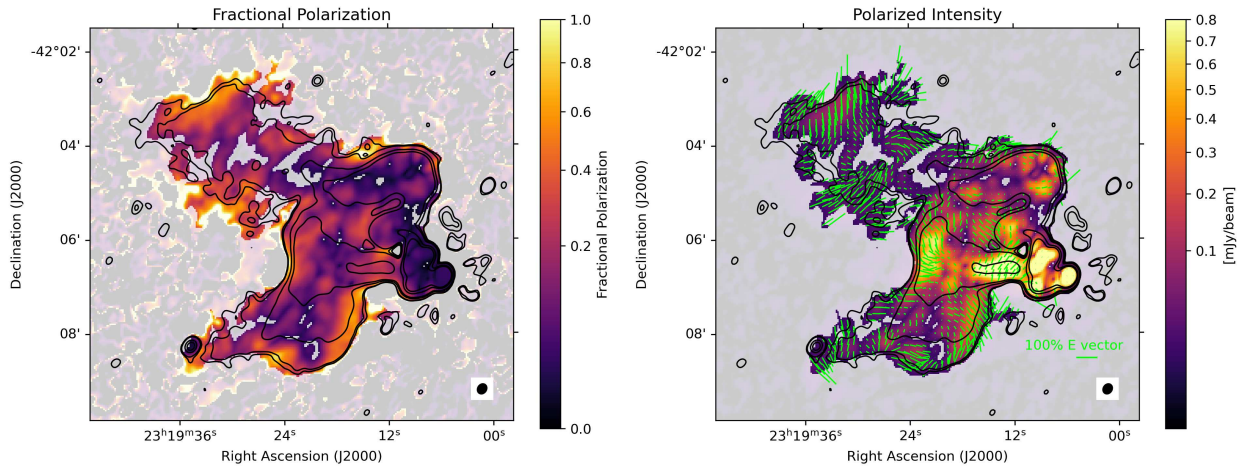


**Figure 31.** Left: Fractional polarization image with a mask computed at  $3\sigma_{QU}$  with  $\sigma_{QU} = 4 \mu\text{Jy}/\text{beam}$ , the constraint of  $0 < f_{\text{pol}} < 1$  and total intensity contours in black. *Right:* Colours of polarized intensity, electric polarization angles in green with lengths proportional to  $f_{\text{pol}}^{0.5}$  and total intensity contours.

It appears that the regions at the end of the northern plume and both in the upper left and lower right of the southern plume present a higher fractional polarization, which would be consistent with a shock-front between the jet and the intra-cluster medium or an adiabatic expansion.

Anyhow, this analysis doesn't take into account all the effect of Faraday rotation and depolarization due to the magnetized ICM which will be better analysed in the next section.

### 7.3.1 Rotation Measure Synthesis

As briefly stated in the previous paragraph, combining all the frequencies into one broadband image of Stokes Q and U leads to misleading interpretations. This is because when the light passes through a magnetized medium, as described in Section 5.2, the linear polarization signal changes, making the polarization angle rotate as a function of wavelength squared due to the Faraday effect as shown in equation 43.

$$\Delta\chi = \text{RM} \cdot \lambda^2 \quad (43)$$

When Q and U are averaged across a wide frequency band, without accounting for this rotation, the result is a depolarized signal which leads to an inaccurate estimate of the intrinsic polarization properties.

To address this, we use rotation measure synthesis, a technique that treats the observed polarization as a Fourier transform of the complex polarization as a function of wavelength squared. RM synthesis reconstructs the polarized emission as a function of Faraday depth by de-rotating channel by channel using Equation 43, leading to a coherent sum of Stokes Q and U.

Following Burn (1966) we start by defining the Faraday Dispersion Function (FDF), which describes the intrinsic polarized flux density per unit Faraday depth  $\phi$  (in  $\text{rad m}^{-2}$ ) and its relationship with the complex polarized emission  $P(\lambda^2)$ , where  $\lambda$  is the wavelength.  $P(\lambda^2)$  can easily be written as a function of the Stokes parameters as  $P = U + iQ$ , while the relationship between the FDF and P is a classic Fourier Transform and is reported in Equation 44:

$$P(\lambda^2) = \int_{-\infty}^{+\infty} F(\phi) e^{2i\phi\lambda^2} d\phi. \quad (44)$$

In order to reconstruct the Faraday Dispersion Function and determine which are the main components that rotates the polarized emission, we need to invert the relationship as:

$$F(\phi) = \frac{1}{\pi} \int_{-\infty}^{+\infty} P(\lambda^2) e^{-2i\phi\lambda^2} d\lambda^2. \quad (45)$$

This inversion presents two main problems: the trivial one is that it is not possible to observe negative wavelengths; the second is that we are not able to observe all the positive ones, but only the ones we sampled. The common practice in this cases is to introduce a window function  $M(\lambda^2)$  representative of our sampling and to define the observed polarized emission as:

$$\tilde{P}(\lambda^2) = M(\lambda^2)P(\lambda^2). \quad (46)$$

In the same way as the sampling in the  $uv$ -plane determines the synthesized PSF of an interferometer, the Rotation Measure Spread Function (RMSF) is the Fourier transform of the sampling function in  $\lambda^2$  space, therefore, with  $m$  channels, the RMSF is defined as:

$$RMSF(\phi) = K \sum_{i=1}^m M(\lambda_i^2) e^{-2i\phi(\lambda_i^2 - \lambda_0^2)} \quad (47)$$

Where  $\lambda_0^2$  is the mean of the sampled values between  $\lambda_1^2$  and  $\lambda_m^2$  and  $K$  is the normalizing constant of the window function  $M(\lambda^2)$ . If we assume uniform weights for all the channels the reconstructed Faraday Dispersion Function can be written as:

$$\tilde{F}(\lambda^2) = K \sum_{i=1}^m \tilde{P}(\lambda_i^2) e^{-2i\phi(\lambda_i^2 - \lambda_0^2)} \quad (48)$$

Continuing the analogy with interferometry, we can also set a limit of the maximum observable Faraday depth  $\|\phi_{\max}\|$  which is given in Brentjens and de Bruyn (2005):

$$\|\phi_{\max}\| \approx \frac{\sqrt{3}}{\delta\lambda^2} \quad (49)$$

where  $\delta\lambda^2$  is the binning used for the single images, which in this case is 4 MHz, therefore if we use 0.9 GHz as a lower estimate we obtain:

$$\begin{aligned} \delta\lambda^2 &= \lambda_{0.9 \text{ GHz}}^2 - \lambda_{0.904 \text{ GHz}}^2 = \left(\frac{c}{9 \times 10^8 \text{ Hz}}\right)^2 - \left(\frac{c}{9.04 \times 10^8 \text{ Hz}}\right)^2 \approx 0.00098 \text{ m}^2 \\ \|\phi_{\max}\| &\approx \frac{\sqrt{3}}{0.00098 \text{ m}^2} = 1770 \text{ rad m}^{-2} \end{aligned} \quad (50)$$

There is also an approximation of the FWHM of the main peak of the RMSF computed using the extrema of the considered frequency range, in this case between 0.9 GHz and 1.4 GHz, therefore:

$$\delta\phi \approx \frac{2\sqrt{3}}{\Delta\lambda^2} = \frac{2\sqrt{3}}{(0.33\text{m})^2 - (0.21\text{m})^2} \approx 53.5 \text{ rad m}^{-2} \quad (51)$$

However these two equations works under the assumption of evenly spaced sampled intervals and a contiguous rectangular observation window. In real applications these values are

mainly indications of what we can expect, in this case the sampled points were not even in  $\nu$  space due to the numerous RFI present in that frequency interval.

The initial 125 I, Q and U images produced using WSClean (see Section 6.2.2) were first convolved at the same resolution of  $12.5'' \times 10''$  using the CASA task *imsmooth*. Then the noise of each image was found by isolating the background and computing the standard deviation. Only the images within the  $3\sigma$  of the noise mean were kept, obtaining at the end only 67 channels, whose images were then stacked in a datacube.

After this preparation, *RMTools* (Purcell et al., 2020) was used to implement the RM synthesis. The software computes the FDF, that tells us which are the main rotating components of the polarized signal. If the signal is rotated only by a single foreground screen is said to be Faraday thin and the relationship between  $\Delta\chi$  and  $\lambda^2$  is linear (Equation 43). If instead there are multiple or extended components, rotating or even emitting, the relationship is more complex.

The RM synthesis has been produced using a  $\Delta\phi = 3 \text{ rad m}^{-2}$ , in order to oversample the RMSF, and a range between  $\pm 500 \text{ rad m}^{-2}$ , because a preliminary analysis showed no components exceeding values of  $\pm 150 \text{ rad m}^{-2}$ .

Important quantities computed by the software are the rotation RMSF, the maximum polarized intensity for each pixel, and the Faraday depth at which that value is found.

From the RMSF, presented in Figure 32, it is possible to see that the FWHM is higher than the theoretical one and it also presents high sidelobes. This is expected due to the non uniform sampling caused by the different flagging across the bandwidth.

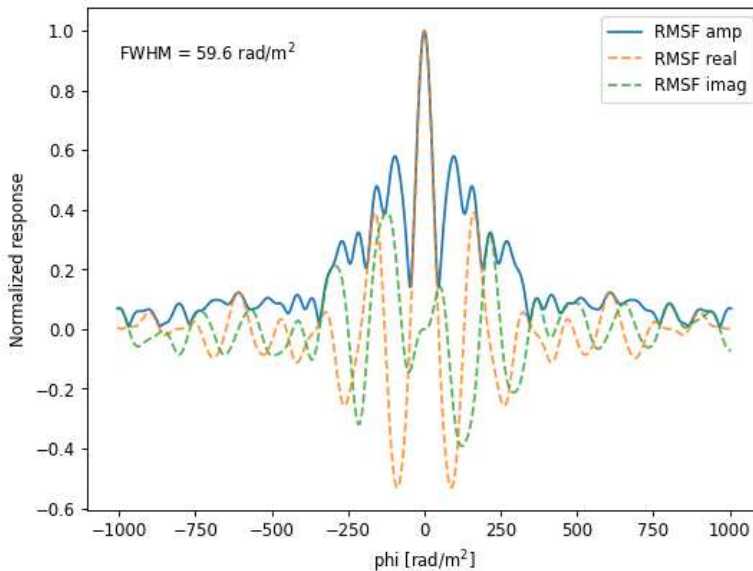


**Figure 32.** The image shows the Rotation Measure Spread Function components and total amplitude.

The maximum value of rotation measure is presented in Figure 33.

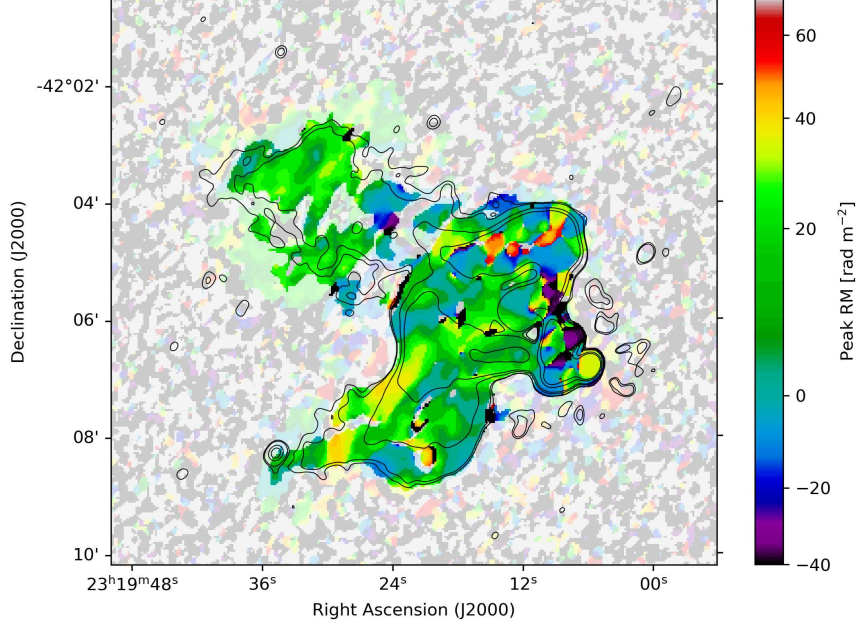


**Figure 33.** The maximum value of rotation measure with a mask at  $4\sigma_{QU}$  with  $\sigma_{QU} = 5 \cdot 10^{-6}$  Jy/beam and total intensity contours.

Following Brentjens and de Bruyn (2005) we can associate an uncertainty on the measured Faraday depth as:

$$\sigma_{\phi} \approx \frac{\text{FWHM}_{\text{RMSF}}}{2 \cdot \text{SNR}} \quad (52)$$

Where  $\text{FWHM}_{\text{RMSF}} = 59.6 \text{ rad m}^{-2}$ , while  $\text{SNR} = \text{MAX\_PI}_{\text{deb}}/\sigma_{QU}$ .

The maximum value of rotation measure in the source oscillates between  $-10 \text{ rad m}^{-2}$  and  $40 \text{ rad m}^{-2}$ , while the one in core the appear to be around  $27.0 \pm 0.1 \text{ rad m}^{-2}$ , a value consistent with the Galactic RM value obtained by Hutschenreuter et al. (2022). This is somehow strange considering that the core should reside in the BCG of a galaxy cluster, therefore, in theory, we should obtain higher values.

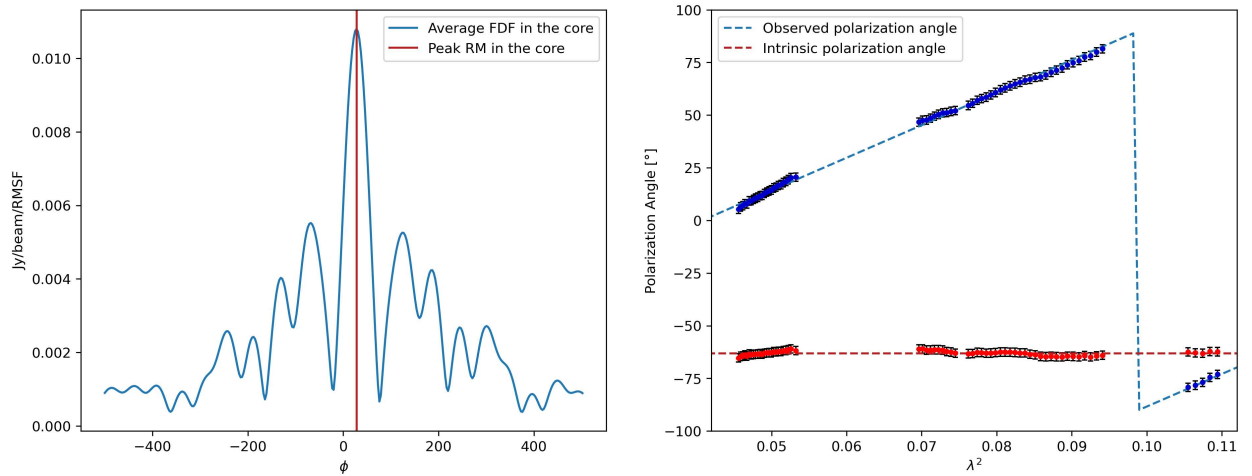


**Figure 34.** *Left:* average FDF in the core, with a prominent peak at  $28 \pm 2 \text{ rad m}^{-2}$ . *Right:* The observed polarization angle plotted against  $\lambda^2$  and the residuals oscillate around the intrinsic polarization value within the errors.

We can also plot the Faraday Dispersion Function in the core to look for multiple components that rotates and  $\Delta\chi$  as a function of  $\lambda^2$ , to verify the linearity. This is presented in Figure 34 and, although the FDF is slightly asymmetric, a single value of RM of  $28 \text{ rad m}^{-2}$  is able to fit the model, with the residuals' scatter within the errors.

In order to produce the fractional polarization we have to remove the bias, originated from the quadrature sum of the noise in Q and U images. However, computing the bias value from the maximum polarization intensity is more complex than before. While in the bandwidth averaged polarization maps produced before we use the Rice distribution, which assumes Gaussian noise in Stokes Q and U, when performing RM synthesis we look for the maximum Polarization across the Faraday Dispersion Function, which fundamentally changes the statistics of the noise.

In this case, the measured peak is not drawn from a single Rice distribution but from the maximum of many correlated noisy samples across Faraday depth. This "search bias" means that the probability of measuring a high polarized signal due purely to noise is significantly larger, and the bias in the recovered amplitude can be much greater than in the previous case, especially at low signal-to-noise ratios.

Following the work done by George et al. (2012), in case of a signal-to-noise ratio greater than 4, the debiased Polarization intensity can be written as:

$$P_{\text{deb}} = \sqrt{(\text{MAX\_PI})^2 - 2.3\sigma_{QU}^2} \quad (53)$$

where  $\sigma_{QU} = (\sigma_Q + \sigma_U)/2$ . This correction mostly affects low-SNR regions; nevertheless, the brightest regions in the debiased RM-synthesis map and the bandwidth averaged map are broadly consistent.

We can now plot again the fractional polarization and electric polarization angles as done before.

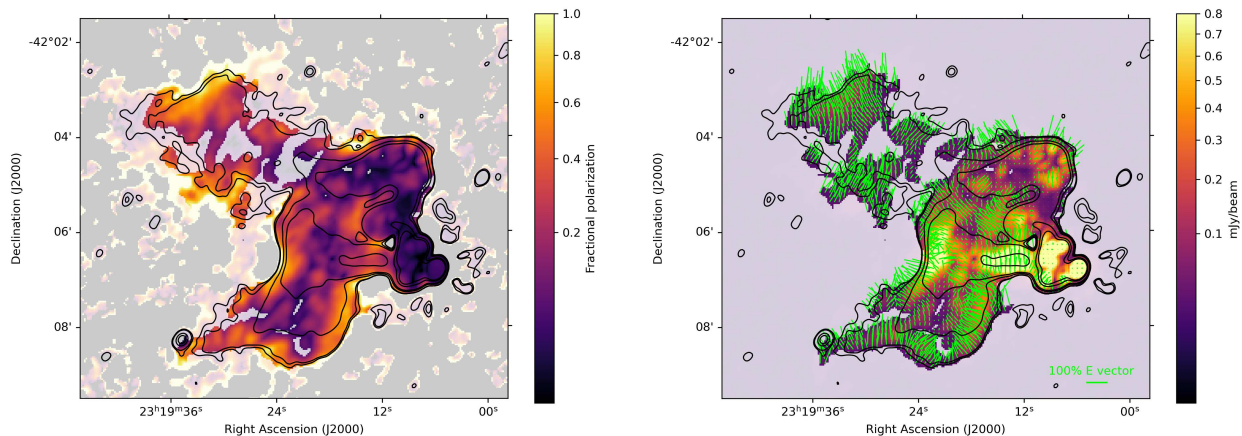


**Figure 35.** *Right:* Fractional polarization image with a mask computed at  $4\sigma_{QU}$  and total intensity contours. *Left:* Debiased maximum polarized intensity, electric polarization angles with lengths proportional to  $f_{\text{pol}}^{0.5}$  and total intensity contours.

We can notice how the fractional polarization of the core increases from values to 3% to 5%, but there is also a general increase across all the radio source, which is expected considering that we are coherently summing the contributions.

Moreover, the electric polarization angles are now perpendicular to the edge of the lobes, which is consistent with the theory that it could be a shock front against the ICM or an

adiabatic expansion (Gabuzda et al., 1992).

Being this object a Blazar, its jets should be aligned with the line of sight, therefore one of them should be further out than the other. Until now, with the analysis performed only with Stokes I images, it is not possible to determine the position along the line of sight.

However, when two opposing jets have different distances, and if the radio galaxy is located within a magnetised plasma, the further jet will suffer more Faraday rotation than the other one.

This effect is called Laing–Garrington effect (Laing, 1988; Garrington et al., 1988), a polarization asymmetry seen in radio galaxies which present two opposite lobes. It arises because the approaching jet is viewed through less magnetized plasma of the galaxy and intracluster medium than the receding jet, which lies behind more depolarizing material along the line of sight. As a result, the further lobe typically shows a lower fractional polarization and a higher rotation measure dispersion.

Detecting this asymmetry can give us a valuable tool to investigate the intracluster medium, impossible to see in X-rays due to the presence of the blazar itself.

The spatial distribution of the fractional polarization is presented separately for the northern and southern emission in Figures 36 and 37.

The radial profiles were computed in concentric annuli centred on the source using a width of 125 kpc. To account for different pixel uncertainties, each pixel  $i$  was assigned a weight  $w_i = 1/\sigma_i^2$ , with  $\sigma_i$  being its RM or fractional polarization uncertainty, depending on the case.

The weighted mean  $\overline{\text{RM}}_w$  and associated error  $\sigma_{\overline{\text{RM}}_w}$  in each annulus were computed as:

$$\begin{aligned} \overline{\text{RM}}_w &= \frac{\sum_i w_i \cdot \text{RM}_i}{\sum_i w_i}, & w_i &= \frac{1}{\sigma_{\text{RM},i}^2} \\ \sigma_{\overline{\text{RM}}_w} &= \sqrt{\frac{1}{\sum_i w_i}} \cdot \sqrt{N_{\text{pixel}/\text{beam}}} \end{aligned} \quad (54)$$

where  $\sigma_{\text{RM},i}$  is the uncertainty on each pixel value, and  $N_{\text{pixel}/\text{beam}}$  is the number of pixels per synthesized beam, in this case 35.4, whose square root we need to multiply in order to consider the correlation of the pixels inside the same beam.

The weighted standard deviation and its associated error were computed using a bootstrap method. Bootstrapping is a resampling technique that allows the estimation of uncertainties directly from the data, without assuming a specific underlying distribution. In this case, the procedure was applied to the set of pixels within each radial annulus as follows:

- For each radial annulus, we considered the original set of pixels with their associated uncertainties.
- A "bootstrap sample" was generated by randomly selecting, with replacement, the same number of pixels as in the original set.
- For each selected pixel, the measured value was perturbed by adding a random value drawn from a Gaussian distribution centred on the measured value and with a standard deviation equal to its associated uncertainty.
- The weighted variance was computed for each perturbed bootstrap sample using the

formula:

$$s_w^2 = \frac{\sum_i w_i (x_i - \bar{x}_w)^2}{\sum_i w_i - \frac{\sum_i w_i^2}{\sum_i w_i}} \quad (55)$$

where  $w_i = 1/\sigma_i^2$  are the inverse-variance weights,  $x_i$  are the pixel values, and  $\bar{x}_w$  is the weighted mean.

- The process was repeated for  $N_{\text{boot}} = 1000$  iterations, producing a distribution of weighted variances.
- The uncertainty on the weighted variance was estimated as the standard deviation of this bootstrap distribution.
- The uncertainty was then multiplied by the  $\sqrt{N_{\text{pixel}/\text{beam}}}$  to account for correlations.

The southern lobe has a more or less constant value of fractional polarization of around  $\sim 25 - 30\%$ . It does not have a visible trend, and the peak at the end is largely affected by the small amount of independent pixels.

The northern lobe instead shows an increase in fractional polarization with distance from the centre, consistent with a depolarizing ICM.

It starts from values around 5% and it increases, reaching values of  $\sim 30 - 40\%$  at the end of the emission.

These former values are affected by the increase of polarized intensity due to the interaction between jets and ICM, and it is not representative of the average value in the bulk of the jet. The average value above 250 kpc can therefore be considered lower, around  $\sim 25 - 30\%$ , and is consistent with the one found in the southern lobe.

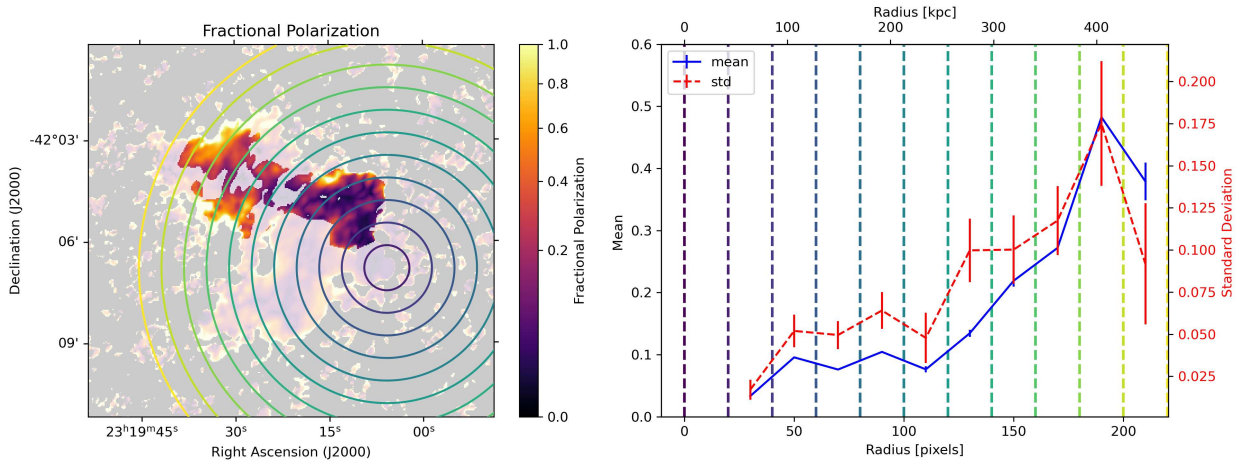


**Figure 36.** Fractional polarization spatial profile computed by isolating the northern part of emission.

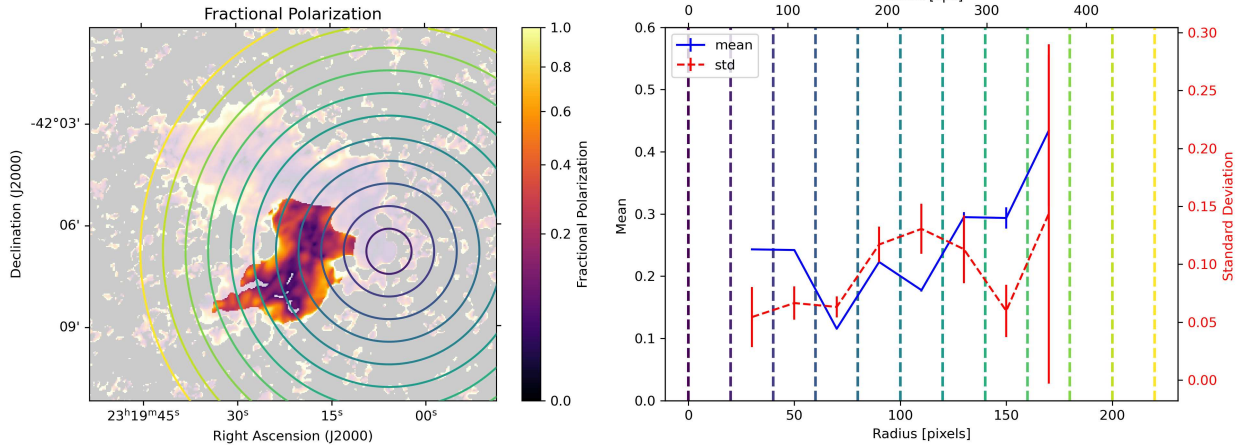


**Figure 37.** Fractional polarization spatial profile computed by isolating the southern part of emission.

Similar considerations can be made for the RM values.

The southern RM profile (Figure 39) is more constant at  $\sim 17 \text{ rad m}^{-2}$ . The variations present are due to the large zone with RM values around  $40 \text{ rad m}^{-2}$ , spatially coincident with the enhancement in fractional polarization. The last annulus is unreliable for the same reason as before.

The northern profile (Figure 38) rises from an almost null mean, to values around  $\sim 16 \text{ rad m}^{-2}$  beyond 300 kpc, while the standard deviation decreases.

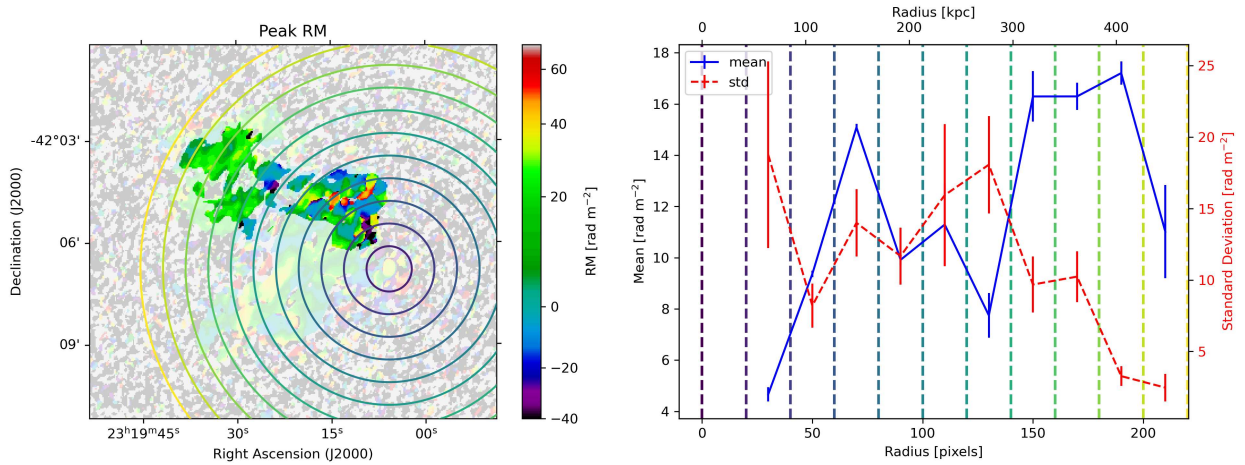


**Figure 38.** Rotation measure spatial profile computed by isolating the northern part of emission.

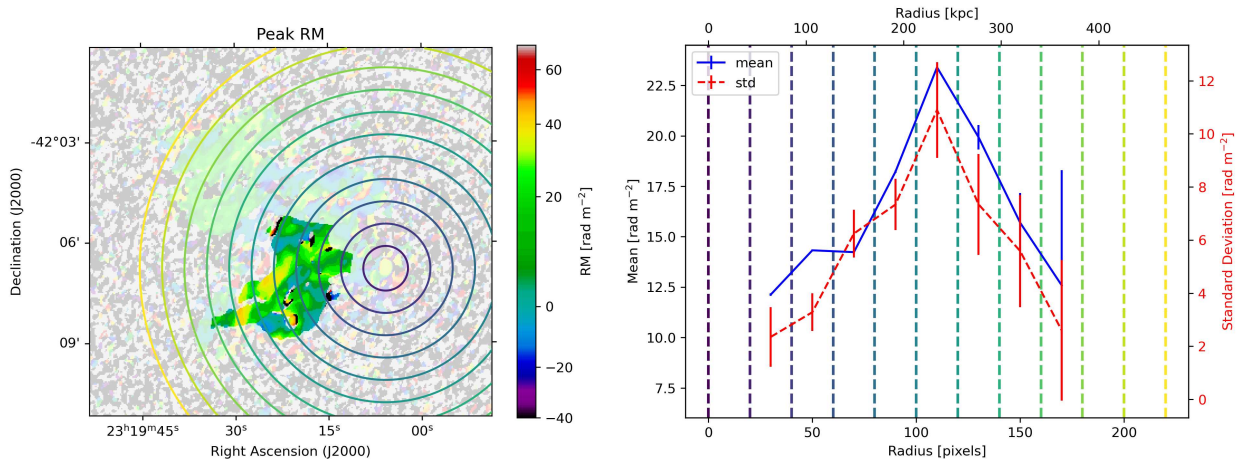


**Figure 39.** Rotation measure spatial profile computed by isolating the southern part of emission.

This analysis allows us to draw some conclusion regarding the morphology of the source along the line of sight.

First, the outermost regions of both lobes, where local Faraday effects are expected to be minimal, yield a mean Faraday depth of  $\sim 16 \text{ rad m}^{-2}$ . While this is lower than the value inferred from the Hutschenreuter, it is consistent (within typical RM uncertainties and spatial variations) with the more recent STAPS (The Southern Twenty-centimetre All-sky Polarization Survey) estimate of  $\sim 14 \text{ rad m}^{-2}$  (Raycheva et al. 2025).

Second, the northern lobe appears to experience a more pronounced effect from the Faraday rotation and depolarization caused by the ICM than the southern one.

The results from the northern jet, especially the trend of the RM standard deviation, appears to be consistent with the typical behaviour from galaxy clusters. A similar result comes from Loi et al. (2025) obtained for the Fornax cluster, an even less massive cluster than this one.

In that work, instead of having a single very extended emission, they made use of multiple background polarized radio sources, creating a grid of RM values.

Overall the behaviour of the source seems consistent with the Laing-Garrington effect, with the northern lobe being in the back and the southern one in the front.

Moreover, the average value of RM in the lobes, where the rotation is minimal, are inconsistent with the one obtained by Hutschenreuter but in agreement with the one from STAPS.

## Conclusions

In this work I performed a spectropolarimetric analysis of the BL Lac object PKS 2316-423 using unpublished MeerKAT data in L-band.

The total intensity analysis presents an object with an unexpected very extended emission. The source has two intricate and undistinguishable jets near the core but become more separated as they move towards the outside. The northern jet measures over 400 kpc in projected length, while the southern one over 300 kpc.

This is strange for this kind of objects, considering that the jets are almost aligned with the line of sight. However, both jets are bent towards one side and appear very twisted.

This strange morphology is probably caused by the interaction with the ICM, being the host galaxy the BCG of the poor galaxy cluster Abell S1111.

Thanks to the high sensitivity reached in this observation, it is possible to perform an in-band spectral map to better study the spectral behaviour of the extended emission.

It is clear that the spectrum steepens steadily going further away from the centre of the emission, starting with a value of  $\alpha \approx -0.2$  (with  $S \propto \nu^\alpha$ ) in the core and reaching values of  $\alpha \approx -1.8$  in the more diffused emission.

To further investigate the ageing of the extended emission, I used the most recent images of the source from the GLEAM and RACS surveys, which I used to compute the integrated flux density and also a measurement present in the AT20G catalogue at 20 GHz.

The integrated spectrum shows a steepening at the highest frequencies, which can be optimally fitted using a CI model, but which contains some issues. The core's behaviour can be characterized using the in-band spectral maps, and the high frequency value is consistent with the source being core dominated.

This suggests that the integrated spectrum cannot be described with a simple CI model but the sum of the contribution of the core and the extended emission needs to be considered. However, the lack of intermediate measurements between 1.25 GHz and 20 GHz does not allow a reliable fit, therefore new observations are needed.

With the injected spectral index found with the CI fit, it is possible to fit the in-band spectral map with a more realistic JP model, and, using some assumption on the magnetic field strength and source morphology, compute the spectral age with a high resolution. This approach leads to ages from 15 Myr near the core, to more than 100 Myr in the more diffused emission.

The polarization analysis was performed by using rotation measure synthesis, which takes into account the Faraday rotation of the electromagnetic waves when travelling through a magnetized plasma, in this case the ICM.

The core appears to have a fractional polarization of about 5%, while the extended emission varies between almost unpolarized signals, up to 40% at the end of the jets.

The polarization angles at the end of the lobes align perpendicularly to the plane of interaction between jets and ICM, as expected.

A deeper analysis consisted in separating the northern and southern jets, to account for the different depolarization effects and RM radial distribution of the Laing-Garrington effect. The southern lobe does not appear to have a trend in the fractional polarization, whose values are around  $\sim 25 - 30\%$ , while the northern lobe increases its fractional polarization from 5 to  $\sim 30 - 40\%$  at the end of the emission.

Similarly, in the southern lobe the RM values have an average of about  $\sim 16 \text{ rad m}^{-2}$ , with an increase spatially coincident with a plane of interaction with the ICM. The northern lobe, instead, presents a decrease of the RM variance from the centre outwards, and an average settling to values of  $\sim 16 - 17 \text{ rad m}^{-2}$  in the furthest part of the emission.

The results from this analysis are consistent with the Laing-Garrington effect, showing a depolarization effect and a larger variance in RM values caused by the rotation effects of the ICM. We can conclude that the southern lobe, being in the front, is less affected by this effect, while the northern one is behind the main bulk of the ICM and can be used as a tool to study the cluster plasma.

The RM values of  $\sim 16 \text{ rad m}^{-2}$  obtained at larger distances should only be affected by the galactic effects and, while they are inconsistent with the work of Hutschenreuter et al. (2022) (of  $\sim 28 \text{ rad m}^{-2}$ ), they are in agreement with the ones from Raycheva et al. (2025) (of  $\sim 14 \text{ rad m}^{-2}$ ).

This analysis displays both the spatial and spectral sensitivity of MeerKAT, allowing us to improve our knowledge on AGN and their interplay with the environment.

Future wideband and higher-resolution spectro-polarimetric studies with MeerKAT will allow us to investigate the magnetic field structure, particle acceleration sites, and jet–environment coupling in even greater detail.

In the future, the enhanced capabilities of the Square Kilometre Array will provide unprecedented sensitivity and resolution, opening a new window on AGN physics across cosmic time and offering critical insights into the role of radio jets in galaxy and cluster evolution.

## References

- Abdollahi, S., Acero, F., Ackermann, M., Ajello, M., Atwood, W. B., Axelsson, M., and Baldini, e. a. (2020). Fermi Large Area Telescope Fourth Source Catalog. *ApJS*, 247(1):33.
- Abell, G. O., Corwin, Jr., H. G., and Olowin, R. P. (1989). A Catalog of Rich Clusters of Galaxies. *ApJS*, 70:1.
- Alexander, P., Brown, M. T., and Scott, P. F. (1984). A multi-frequency radio study of Cygnus A. *MNRAS*, 209:851–868.
- Antonucci, R. (1993). Unified models for active galactic nuclei and quasars. *ARA&A*, 31:473–521.
- Baldi, R. D., Capetti, A., and Giovannini, G. (2015). Pilot study of the radio-emitting AGN population: the emerging new class of FR 0 radio-galaxies. *A&A*, 576:A38.
- Beckmann, V. and Shrader, C. R. (2012). *Active Galactic Nuclei*.
- Blandford, R. D. and Payne, D. G. (1982). Hydromagnetic flows from accretion disks and the production of radio jets. *MNRAS*, 199:883–903.
- Blandford, R. D. and Znajek, R. L. (1977). Electromagnetic extraction of energy from Kerr black holes. *MNRAS*, 179:433–456.
- Blumenthal, G. R. and Gould, R. J. (1970). Bremsstrahlung, Synchrotron Radiation, and Compton Scattering of High-Energy Electrons Traversing Dilute Gases. *Reviews of Modern Physics*, 42(2):237–271.
- Bolli, P., Orlati, A., Stringhetti, L., Orfei, A., and et al., R. (2015). Sardinia Radio Telescope. *Journal of Astronomical Instrumentation*, 4:1550008–880.
- Brentjens, M. A. and de Bruyn, A. G. (2005). Faraday rotation measure synthesis. *A&A*, 441(3):1217–1228.
- Burn, B. J. (1966). On the depolarization of discrete radio sources by faraday dispersion. *Monthly Notices of the Royal Astronomical Society*, 133(1):67–83.
- Buttiglione, S., Capetti, A., Celotti, A., Axon, D. J., Chiaberge, M., Macchetto, F. D., and Sparks, W. B. (2010). An optical spectroscopic survey of the 3CR sample of radio galaxies with  $z < 0.3$ . II. Spectroscopic classes and accretion modes in radio-loud AGN. *A&A*, 509:A6.
- Capetti, A. and Raiteri, C. M. (2015). Looking below the floor: constraints on the agn radio luminosity functions at low power. *Monthly Notices of the Royal Astronomical Society: Letters*, 449(1):L128–L131.
- Cassaro, P., Stanghellini, C., Bondi, M., Dallacasa, D., Della Ceca, R., and Zappalà, R. A. (1999). Extended radio emission in bl lac objects - i. the images. *Astron. Astrophys. Suppl. Ser.*, 139(3):601–616.
- Cicone, C., Maiolino, R., Sturm, E., and et al., G. (2014). Massive molecular outflows and evidence for AGN feedback from CO observations. *aap*, 562:A21.

- Crawford, C. S. and Fabian, A. C. (1994). A non-thermal radio/optical/x-ray source in pks 2316 – 423. *Monthly Notices of the Royal Astronomical Society*, 266(3):669–677.
- de Gasperin, F., Rudnick, L., Finoguenov, A., and et al., W. (2022). Meerkat view of the diffuse radio sources in abell 3667 and their interactions with the thermal plasma. *AA*, 659:A146.
- Dekel, A. and Ostriker, J. P., editors (1999). *Formation of Structure in the Universe*.
- Drinkwater, M. J., Gregg, M. D., and Colless, M. (2001). Substructure and Dynamics of the Fornax Cluster. *ApJL*, 548(2):L139–L142.
- Einasto, Maret, Einasto, Jaan, Tenjes, Peeter, Korhonen, Suvi, Kipper, Rain, Tempel, Elmo, Liivamägi, Lauri Juhan, and Heinämäki, Pekka (2024). Galaxy groups and clusters and their brightest galaxies within the cosmic web. *AA*, 681:A91.
- Fabian, A. C. (2003). Reverberation revisited. In Hasinger, G., Boller, T., and Parmer, A. N., editors, *XEUS - studying the evolution of the hot universe*, page 207.
- Fabian, A. C. (2012). Observational Evidence of Active Galactic Nuclei Feedback. *ARA&A*, 50:455–489.
- Fanaroff, B. L. and Riley, J. M. (1974). The morphology of extragalactic radio sources of high and low luminosity. *MNRAS*, 167:31P–36P.
- Farnes, J. S., Green, D. A., and Kantharia, N. G. (2014). Spectropolarimetry with the Giant Metrewave Radio Telescope at 610 MHz: a case study of two southern compact group fields. *MNRAS*, 437(4):3236–3254.
- Ferrarese, L. and Merritt, D. (2000). A Fundamental Relation between Supermassive Black Holes and Their Host Galaxies. *ApJL*, 539(1):L9–L12.
- Gabuzda, D. C., Cawthorne, T. V., Roberts, D. H., and Wardle, J. F. C. (1992). A survey of the milliarcsecond polarization properties of BL Lacertae objects at 5 GHz. *ApJ*, 388:40–54.
- Ganguly, R. and Brotherton, M. S. (2007). What Fraction of Active Galaxies Actually Show Outflows? In *American Astronomical Society Meeting Abstracts*, volume 211 of *American Astronomical Society Meeting Abstracts*, page 75.03.
- Garrington, S. T., Leahy, J. P., Conway, R. G., and Laing, R. A. (1988). A systematic asymmetry in the polarization properties of double radio sources with one jet. *Nature*, 331(6152):147–149.
- George, S. J., Stil, J. M., and Keller, B. W. (2012). Detection Thresholds and Bias Correction in Polarized Intensity. *PASA*, 29(3):214–220.
- Gitti, M., Brighenti, F., and McNamara, B. R. (2012). Evidence for AGN Feedback in Galaxy Clusters and Groups. *Advances in Astronomy*, 2012:950641.
- Glowacki, M., Allison, J. R., Sadler, E. M., Moss, V. A., Curran, S. J., Musaeva, A., Deng, C., Parry, R., and Sligo, M. C. (2017). H i absorption in nearby compact radio galaxies. *Monthly Notices of the Royal Astronomical Society*, 467(3):2766–2786.

- Gopal-Krishna and Wiita, P. J. (2000). Extragalactic radio sources with hybrid morphology: implications for the Fanaroff-Riley dichotomy. *A&A*, 363:507–516.
- Govoni, F. and Feretti, L. (2004). Magnetic Fields in Clusters of Galaxies. *International Journal of Modern Physics D*, 13(8):1549–1594.
- Govoni, F., Feretti, L., Giovannini, G., Dallacasa, D., and Taylor, G. B. (2002). Magnetic Fields in Clusters of Galaxies. In Gilfanov, M., Sunyeav, R., and Churazov, E., editors, *Lighthouses of the Universe: The Most Luminous Celestial Objects and Their Use for Cosmology*, page 78.
- Hopkins, P. F. and Hernquist, L. (2006). Fueling Low-Level AGN Activity through Stochastic Accretion of Cold Gas. *ApJS*, 166(1):1–36.
- Hugo, B. V., Perkins, S., Merry, B., Mauch, T., and Smirnov, O. M. (2022). Tricolour: an optimized sunthreshold flagger for meerkat.
- Hutschenreuter, S., Anderson, C. S., Betti, S., and et al., B. (2022). The Galactic Faraday rotation sky 2020. *A&A*, 657:A43.
- Jaffe, W. J. and Perola, G. C. (1973). Dynamical Models of Tailed Radio Sources in Clusters of Galaxies. *A&A*, 26:423.
- Jones, D. H., Saunders, W., Colless, M., and et al., R. (2004). The 6dF Galaxy Survey: samples, observational techniques and the first data release. *MNRAS*, 355(3):747–763.
- Jones, P. A. and McAdam, W. B. (1992). The Structure of Southern Extragalactic Radio Sources. *ApJS*, 80:137.
- Józsa, G. I. G., Andati, L. A. L., and et Al., d. (2022). CARACal - The Containerized Automated Radio Astronomy Calibration Pipeline. In Ruiz, J. E., Pierfederci, F., and Teuben, P., editors, *Astronomical Data Analysis Software and Systems XXX*, volume 532 of *Astronomical Society of the Pacific Conference Series*, page 447.
- Kellermann, K. I., Sramek, R., Schmidt, M., Shaffer, D. B., and Green, R. (1989). VLA Observations of Objects in the Palomar Bright Quasar Survey. *AJ*, 98:1195.
- Kharb, P., Lister, M. L., and Cooper, N. J. (2010). Extended Radio Emission in MOJAVE Blazars: Challenges to Unification. *ApJ*, 710(1):764–782.
- King, A. R. and Pounds, K. A. (2003). Black hole winds. *MNRAS*, 345(2):657–659.
- Kormendy, J. and Ho, L. C. (2013). Coevolution (Or Not) of Supermassive Black Holes and Host Galaxies. *ARA&A*, 51(1):511–653.
- Laing, R. A. (1988). The sidedness of jets and depolarization in powerful extragalactic radio sources. *Nature*, 331(6152):149–151.
- Laing, R. A., Bridle, A. H., Parma, P., Feretti, L., Giovannini, G., Murgia, M., and Perley, R. A. (2008). Multifrequency VLA observations of the FR I radio galaxy 3C 31: morphology, spectrum and magnetic field. *MNRAS*, 386(2):657–672.
- Li, F., Brown, S., Cornwell, T. J., and de Hoog, F. (2011). The application of compressive sampling to radio astronomy - ii. faraday rotation measure synthesis. *AA*, 531:A126.

- Loi, F., Serra, P., Murgia, M., Govoni, F., Vacca, V., Maccagni, F., Kleiner, D., and Kamphuis, P. (2025). The MeerKAT Fornax Survey: IV. A close look at the cluster physics through the densest rotation measure grid. *A&A*, 694:A125.
- Maccacaro, T., Perola, G. C., and Elvis, M. (1981). X-Ray Observations of Emission Line Galaxies with the Einstein Observatory. *Space Sci. Rev.*, 30(1-4):61–65.
- Marscher, A., Jorstad, S., and et al., D. (2008). The inner jet of an active galactic nucleus as revealed by a radio-to-ray outburst. *Nature*, 452:966–9.
- Massaro, F., Thompson, D. J., and Ferrara, E. C. (2015). The extragalactic gamma-ray sky in the Fermi era. *A&ARv*, 24:2.
- Mauch, T., Cotton, W. D., Condon, J. J., and et al., M. (2020). The 1.28 ghz meerkat deep2 image. *The Astrophysical Journal*, 888(2):61.
- McConnell, D., Hale, C. L., Lenc, E., Banfield, J. K., and et al., H. (2020). The Rapid ASKAP Continuum Survey I: Design and first results. *PASA*, 37:e048.
- McNamara, B. R. and Nulsen, P. E. J. (2007). Heating Hot Atmospheres with Active Galactic Nuclei. *ARA&A*, 45(1):117–175.
- Mills, B. Y. (1981). The Molonglo Observatory synthesis telescope. *PASA*, 4(2):156–159.
- Mooney, S., Massaro, F., Quinn, J., and et al., C. (2021). Characterising the extended morphologies of bl lacertae objects at 144 mhz with lofar. *The Astrophysical Journal Supplement Series*, 257(2):30.
- Muller, A., Poggianti, B. M., Pfrommer, C., and et al., A. (2021). Highly ordered magnetic fields in the tail of the jellyfish galaxy JO206. *Nature Astronomy*, 5:159–168.
- Murgia, M., Fanti, C., Fanti, R., Gregorini, L., Klein, U., Mack, K. H., and Vigotti, M. (1999). Synchrotron spectra and ages of compact steep spectrum radio sources. *A&A*, 345:769–777.
- Murgia, M., Parma, P., Mack, K.-H., de Ruiter, H. R., Fanti, R., Govoni, F., Tarchi, A., Giacintucci, S., and Markevitch, M. (2011). Dying radio galaxies in clusters. *AA*, 526:A148.
- Murphy, T., Sadler, E. M., and et al., E. (2010). The Australia Telescope 20 GHz Survey: the source catalogue. *MNRAS*, 402(4):2403–2423.
- O’Dea, C. P. and Saikia, D. J. (2021). Compact steep-spectrum and peaked-spectrum radio sources. *A&A*, 29(1):3.
- Oei, M., Van Weeren, R., Rottgering, H., Stern, D., and Djorgovski, S. (2024). Black hole jets on the scale of the Cosmic Web. In *American Astronomical Society Meeting Abstracts*, volume 243 of *American Astronomical Society Meeting Abstracts*, page 425.08.
- Offringa, A. R. (2010). AOflogger: RFI Software. Astrophysics Source Code Library, record ascl:1010.017.
- Padovani, P., Alexander, D. M., Assef, R. J., De Marco, B., Giommi, P., Hickox, R. C., Richards, G. T., Smolčić, V., Hatziminaoglou, E., Mainieri, V., and Salvato, M. (2017). Active galactic nuclei: what’s in a name? *A&ARv*, 25(1):2.

- Padovani, P. and Giommi, P. (1995). The Connection between X-Ray- and Radio-selected BL Lacertae Objects. *ApJ*, 444:567.
- Pajdosz-Śmierciak, U., Śmierciak, B., and Jamrozy, M. (2022). Possible jet reorientation in low-frequency radio structures of blazars. *Monthly Notices of the Royal Astronomical Society*, 514(2):2122–2134.
- Parma, P., Murgia, M., Morganti, R., Capetti, A., de Ruiter, H. R., and Fanti, R. (1999). Radiative ages in a representative sample of low luminosity radio galaxies. *A&A*, 344:7–16.
- Pasetto, A., Carrasco-González, C., and et al., G. (2021). Reading m87’s dna: A double helix revealing a large-scale helical magnetic field. *The Astrophysical Journal Letters*, 923(1):L5.
- Purcell, C. R., Van Eck, C. L., West, J., Sun, X. H., and Gaensler, B. M. (2020). RM-Tools: Rotation measure (RM) synthesis and Stokes QU-fitting. Astrophysics Source Code Library, record ascl:2005.003.
- Rafferty, D. A., McNamara, B. R., Nulsen, P. E. J., and Wise, M. W. (2006). The Feedback-regulated Growth of Black Holes and Bulges through Gas Accretion and Starbursts in Cluster Central Dominant Galaxies. *ApJ*, 652(1):216–231.
- Ramatsoku, M., Murgia, M., and et al., V. (2020). Collimated synchrotron threads linking the radio lobes of eso 137-006. *aap*, 636:L1.
- Raycheva, N., Haverkorn, M., Ideguchi, S., and et al., S. (2025). Faraday moments of the Southern Twenty-centimeter All-sky Polarization Survey (STAPS). *A&A*, 695:A101.
- Rupke, D. S. N. and Veilleux, S. (2011). Integral Field Spectroscopy of Massive, Kiloparsec-scale Outflows in the Infrared-luminous QSO Mrk 231. *ApJL*, 729(2):L27.
- Rybicki, G. B. and Lightman, A. P. (1979). *Radiative processes in astrophysics*.
- Sarazin, C. L. (2002). The Physics of Cluster Mergers. In Feretti, L., Gioia, I. M., and Giovannini, G., editors, *Merging Processes in Galaxy Clusters*, volume 272 of *Astrophysics and Space Science Library*, pages 1–38.
- Saripalli, L. (2012). Understanding the Fanaroff-Riley Radio Galaxy Classification. *ApJS*, 144(3):85.
- Schmidt, M. (1963). 3C 273 : A Star-Like Object with Large Red-Shift. *Nature*, 197(4872):1040.
- Serra, P., Westmeier, T., Giese, N., Jurek, R., Flöer, L., Popping, A., Winkel, B., van der Hulst, T., Meyer, M., Koribalski, B. S., Staveley-Smith, L., and Courtois, H. (2015). Sofia: a flexible source finder for 3d spectral line data. *Monthly Notices of the Royal Astronomical Society*, 448(2):1922–1929.
- Seyfert, C. K. (1943). Nuclear Emission in Spiral Nebulae. *ApJ*, 97:28.
- Sihlangu, I., Oozeer, N., and Bassett, B. (2022). Nature and evolution of uhf and l-band radio frequency interference at the meerkat radio telescope.

- Slee, O. B. (1995). Radio sources observed with the Culgoora circular array. *Australian Journal of Physics*, 48:143–186.
- Springel, V., White, S. D. M., and et al., J. (2005). Simulations of the formation, evolution and clustering of galaxies and quasars. *Nature*, 435(7042):629–636.
- Stocke, J. T., Morris, S. L., Gioia, I. M., Maccacaro, T., Schild, R., Wolter, A., Fleming, T. A., and Henry, J. P. (1991). The Einstein Observatory Extended Medium-Sensitivity Survey. II. The Optical Identifications. *ApJS*, 76:813.
- Stroe, A., Catlett, V., Harwood, J. J., Vernstrom, T., and Mingo, B. (2022). The Host Galaxies of Hybrid Morphology Radio Sources. *ApJ*, 941(2):136.
- Su, K.-Y., Hopkins, P. F., Hayward, C. C., Ma, X., Faucher-Giguère, C.-A., Kereš, D., Orr, M. E., Chan, T. K., and Robles, V. H. (2019). The failure of stellar feedback, magnetic fields, conduction, and morphological quenching in maintaining red galaxies. *MNRAS*, 487(3):4393–4408.
- Taylor, A. and Legodi, S. (2024). A meerkat polarization survey of southern calibration sources. *The Astronomical Journal*, 167:273.
- Urry, C. M. and Padovani, P. (1995). Unified Schemes for Radio-Loud Active Galactic Nuclei. *PASP*, 107:803.
- Van der Tol, S., Veenboer, B., and Offringa, A. R. (2018). Image domain gridding: a fast method for convolutional resampling of visibilities. *Astronomy & Astrophysics*, 616:A27.
- van Weeren, R. J., de Gasperin, F., Akamatsu, H., Brügger, M., Feretti, L., Kang, H., Stroe, A., and Zandanel, F. (2019). Diffuse Radio Emission from Galaxy Clusters. *Space Sci. Rev.*, 215(1):16.
- Wang, D.-X., Ye, Y.-C., Li, Y., and Ge, Z.-J. (2008). The bz–mc–bp model for jet production from a black hole accretion disc. *Monthly Notices of the Royal Astronomical Society*, 385(2):841–848.
- Wayth, R. B., Lenc, E., Bell, M. E., and et al., C. (2015). GLEAM: The GaLactic and Extragalactic All-Sky MWA Survey. *PASA*, 32:e025.
- Wen, Z. L. and Han, J. L. (2024). VizieR Online Data Catalog: Galaxy clusters from DESI Legacy Surveys & WISE (Wen+, 2024). VizieR On-line Data Catalog: J/ApJS/272/39. Originally published in: 2024ApJS..272...39W.
- Wright, A. and Otrupcek, R. (1990). Parkes Catalog, 1990, Australia telescope national facility. *PKS Catalog (1990)*, page 0.
- Xue, S.-J., Zhang, Y.-H., and Chen, J.-S. (2000). Rosat/asca observations of a serendipitous bl lacertae object pks 2316–423: The variable high-energy tail of synchrotron radiation. *The Astrophysical Journal*, 538(1):121.
- Zabludoff, A. I. and Mulchaey, J. S. (1998). The Properties of Poor Groups of Galaxies. I. Spectroscopic Survey and Results. *ApJ*, 496(1):39–72.